

This is an Open Access document downloaded from ORCA, Cardiff University's institutional repository:<https://orca.cardiff.ac.uk/id/eprint/120132/>

This is the author's version of a work that was submitted to / accepted for publication.

Citation for final published version:

Townsend, Meredith, Huber, Christian, Degruyter, Wim and Bachmann, Olivier 2019. Magma chamber growth during inter-caldera periods: insights from thermo-mechanical modeling with applications to Laguna del Maule, Campi Flegrei, Santorini, and Aso. *Geochemistry, Geophysics, Geosystems* 20 (3) , pp. 1574-1591. 10.1029/2018GC008103

Publishers page: <http://dx.doi.org/10.1029/2018GC008103>

Please note:

Changes made as a result of publishing processes such as copy-editing, formatting and page numbers may not be reflected in this version. For the definitive version of this publication, please refer to the published source. You are advised to consult the publisher's version if you wish to cite this paper.

This version is being made available in accordance with publisher policies. See <http://orca.cf.ac.uk/policies.html> for usage policies. Copyright and moral rights for publications made available in ORCA are retained by the copyright holders.



1 Magma chamber growth during inter-caldera periods: insights from thermo-
2 mechanical modeling with applications to Laguna del Maule, Campi Flegrei,
3 Santorini, and Aso
4

5 Meredith Townsend ^{a,b}*, Christian Huber ^a, Wim Degruyter ^c, Olivier Bachmann ^d

6 ^a Department of Earth, Environmental, and Planetary Sciences, Brown University, 324 Brook
7 Street, Providence, RI 02906, USA

8 ^b Department of Earth Sciences, University of Oregon, 100 Cascade Hall, Eugene, OR 97403,
9 USA

10 ^c School of Earth and Ocean Sciences, Cardiff University, Main Building, Park Place, Cardiff,
11 CF10 3AT, United Kingdom

12 ^d Department of Earth Sciences, ETH Zurich, Sonneggstrasse 5, 8092 Zurich, Switzerland
13

14 *Keywords:* Magma chambers, caldera cycles, eruption frequency, eruption volume, magmatic
15 volatiles

16 *Key points:*

- 17 • Coupled thermo-mechanical modeling suggests that magma chambers grow when
18 recharge and viscous relaxation of the crust are fast compared to chamber cooling
- 19 • Magma chambers containing exsolved volatiles may shrink over time despite constant
20 recharge because high magma compressibility leads to large eruption volumes
- 21 • Eruptive phases at Laguna del Maule, Campi Flegrei, Santorini and Aso reflect growth of
22 chambers; amount of growth can be estimated from eruption frequency and size

23
24 * Corresponding author: Tel.: +1 434 390-7952

25 *E-mail addresses:* meredith_townsend@brown.edu (M.R. Townsend),

26 christian_huber@brown.edu (C. Huber), degruyterw@cardiff.ac.uk (W. Degruyter),

27 olivier.bachmann@erdw.ethz.ch (O. Bachmann)

28 **Abstract**

29 Crustal magma chambers can grow to be hundreds to thousands of cubic kilometers, potentially
30 feeding catastrophic caldera-forming eruptions. Smaller-volume chambers are expected to erupt
31 frequently and freeze quickly; a major outstanding question is how magma chambers ever grow
32 to the sizes required to sustain the largest eruptions on Earth. We use a thermo-mechanical model
33 to investigate the primary factors that govern the extrusive:intrusive ratio in a chamber, and how
34 this relates to eruption frequency, eruption size, and long-term chamber growth. The model
35 consists of three fundamental timescales: the magma injection timescale τ_{in} , the cooling
36 timescale τ_{cool} , and the timescale for viscous relaxation of the crust τ_{relax} . We estimate these
37 timescales using geologic and geophysical data from four volcanoes (Laguna del Maule, Campi
38 Flegrei, Santorini, Aso) to compare them with the model. In each of these systems, τ_{in} is much
39 shorter than τ_{cool} and slightly shorter than τ_{relax} , conditions that in the model are associated with
40 efficient chamber growth and simultaneous eruption. In addition, the model suggests that the
41 magma chambers underlying these volcanoes are growing at rates between $\sim 10^{-4}$ - 10^{-2} km³/yr,
42 speeding up over time as the chamber volume increases. We find scaling relationships for
43 eruption frequency and size that suggest that as chambers grow and volatiles exsolve, eruption
44 frequency decreases but eruption size increases. These scaling relationships provide a good
45 match to the eruptive history from the natural systems, suggesting the relationships can be used
46 to constrain chamber growth rates and volatile saturation state from the eruptive history alone.

47

48 *Plain Language Summary*

49 Magma chambers in the earth's crust grow by incremental addition of new magma from deeper
50 reservoirs, and over time can reach volumes that would fill the entire Grand Canyon. However,
51 small magma chambers in the earliest stages of formation are prone to frequent eruptions and
52 will lose heat quickly to the surrounding crust, both of which supposedly impede growth.
53 Therefore, an important question is how magma chambers can possibly grow to such large sizes.
54 Here, we present results of physics-based modeling aimed at understanding what conditions
55 allow magma chambers to grow. We test effects of chamber size, rate of magma supply, water
56 content in the magma, and plasticity of the crust hosting the chamber. Results suggest that
57 growth is promoted when chambers cool slowly and are hosted within pliable crust that can
58 easily relax pressures that build within the chamber. Surprisingly, we found that for a particular
59 range of crustal pliability, growth is accompanied by frequent volcanic eruptions. We compared
60 these results to four large volcanoes in Chile, Italy, Greece, and Japan. Model predictions for
61 eruption frequency and chamber growth rates are a good match to what we observe at these
62 volcanoes from the rock record and active monitoring systems.

63

64

65 1. Introduction

66 The growth of crustal magma chambers largely governs the frequency and size of
67 volcanic eruptions and plays a critical role in the thermal and chemical evolution of the planet.
68 Field studies of plutons ([C. F. Miller et al., 2011](#); [R. B. Miller & Paterson, 2001](#); [Paterson &
69 Miller, 1998](#); [Wiebe, 1994](#); [Wiebe & Collins, 1998](#)) and eruptive deposits ([Chamberlain, Wilson,
70 Wooden, Charlier, & Ireland, 2014](#); [Charlier, Wilson, & Davidson, 2008](#); [Matthews, Vazquez, &
71 Calvert, 2015](#)), analogue experiments ([Snyder & Tait, 1995](#)), and numerical models ([Annen,
72 2009](#); [Jellinek & DePaolo, 2003](#); [Karlstrom, Dufek, & Manga, 2009](#)) have illuminated the
73 physical processes by which magma chambers are assembled, typically by the episodic injection
74 of magma via dikes ascending from deeper reservoirs. However, we do not yet understand what
75 determines the proportion of magma that ultimately remains in the crust relative to the amount
76 erupted ([Black & Manga, 2016](#); [White, Crisp, & Spera, 2006](#)) and how this relates to the long-
77 term growth of eruptible portions of the reservoir, referred to here as magma chambers. Thermal
78 and mechanical models ([Annen, 2009](#); [Degruyter & Huber, 2014](#); [Jellinek & DePaolo, 2003](#))
79 suggest that for a given rate of magma supply, smaller chambers are more likely to erupt and
80 freeze, while larger chambers favor magma storage, which begs the question: How do magma
81 chambers grow to the volumes required to sustain the largest eruptions on Earth?

82 Large silicic volcanoes are capable of erupting hundreds to thousands of cubic kilometers
83 of material, typically accompanied by catastrophic collapse of the magma chamber roof to form
84 a caldera ([de Silva & Gregg, 2014](#); [W. Hildreth, 1981](#); [Lipman, Steven, & Mehnert, 1970](#);
85 [Sparks et al., 1985](#)). These caldera-forming events can occur multiple times at the same volcano
86 but typically happen infrequently, separated by tens to hundreds of thousands of years
87 ([Bevilacqua et al., 2018](#); [Christiansen, 2001](#); [Druitt & Francaviglia, 1992](#); [Kaneko, Kamata,
88 Koyaguchi, Yoshikawa, & Furukawa, 2007](#); [Orsi, DeVita, & diVito, 1996](#); [Wilson et al., 1995](#)).
89 Following large caldera-forming events, eruptions tend to be smaller-volume and higher-
90 frequency, indicating a significant reduction in chamber size ([Degruyter, Huber, Bachmann,
91 Cooper, & Kent, 2016](#); [Forni, Degruyter, Bachmann, De Astis, & Mollo, 2018](#); [Parks et al.,
92 2012](#); [Singer et al., 2014](#)). In this study, we focus on how small-volume post-caldera magma
93 chambers grow to the sizes that host catastrophic caldera-forming eruptions, with a particular
94 interest in the following questions: What controls the growth rates of magma chambers and the

95 time between catastrophic caldera-forming events? How does growth of the magma chamber
96 relate to the frequency and size distribution of eruptions that occur during the inter-caldera
97 period, and is there any way to use these eruptive characteristics to infer where a volcano is in its
98 caldera cycle?

99 Growth of crustal chambers undeniably requires a sustained supply of magma; however,
100 we posit that the partitioning of ascending magma between the surface and crust (the ratio of
101 mass erupted to added, $M_{er}:M_{add}$) is also governed by the mechanics of the magma chamber.
102 Degruyter and Huber (2014) constructed a thermo-mechanical framework to study the frequency
103 of eruptions originating from shallow chambers fed by a supply of magma. The framework
104 compares timescales for magma injection, cooling, and viscous relaxation of the surrounding
105 crust:

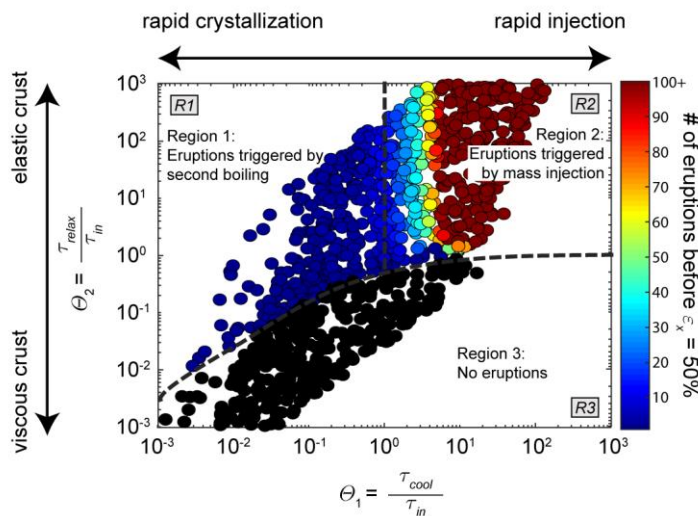
$$106 \quad \tau_{in} = \frac{\rho V}{\dot{M}_{in}} \quad (1)$$

$$107 \quad \tau_{cool} = \frac{R^2}{\kappa} \quad (2)$$

$$108 \quad \tau_{relax} = \frac{\eta_r}{\Delta P_c} \quad (3)$$

109
110
111
112 where the governing parameters include the chamber volume $V = \frac{4}{3}\pi R^3$, bulk magma density ρ ,
113 mass recharge rate \dot{M}_{in} , thermal diffusivity κ , host-rock viscosity η_r , and the critical
114 overpressure in the chamber required to initiate an eruption ΔP_c (Rubin, 1995). Eruptions are
115 typically envisaged as the result of magma recharge that is large enough and rapid enough to
116 both pressurize the chamber and prevent solidification (Annen, 2009; Gelman, Gutierrez, &
117 Bachmann, 2013; Jellinek & DePaolo, 2003). In other words, an eruption may be triggered if
118 $\tau_{in} < \tau_{relax}$ and $\tau_{in} < \tau_{cool}$. However, eruptions also may be triggered by the exsolution of
119 magmatic volatiles during crystallization and second boiling, (Black & Manga, 2017; Blake,
120 1984; Forni et al., 2018; M. J. Stock, Humphreys, Smith, Isaia, & Pyle, 2016; Tait, Jaupart, &

121 [Vergnolle, 1989](#)), which generally would occur when $\tau_{cool} < \tau_{in}$ and $\tau_{cool} < \tau_{relax}$. We can
 122 visualize the eruption mechanisms and eruption frequency as a function of the fundamental
 123 timescales using a regime diagram from Degruyter and Huber ([2014](#)) shown in Figure 1. In the
 124 diagram, $\theta_1 = \frac{\tau_{cool}}{\tau_{in}}$ and $\theta_2 = \frac{\tau_{relax}}{\tau_{in}}$. Eruptions triggered by second boiling occur when cooling is
 125 the fastest process and the crust behaves elastically (Region 1, $\theta_1 < 1$ and $\theta_2 > \theta_1$). Eruptions
 126 triggered by mass injection occur when injection is faster than cooling and the crust behaves
 127 elastically (Region 2, $\theta_1 > 1$ and $\theta_2 > 1$). Finally, no eruptions are predicted to occur if crustal
 128 relaxation is faster than both cooling and injection (Region 3).



129 **Figure 1.** Regime diagram modified from Degruyter and Huber ([2014](#)) showing the relationship between eruption
 130 frequency and triggering mechanism, and the timescales for magma recharge, chamber cooling, and viscous
 131 relaxation of the host rock. Circles are colored by the number of eruptions that occur before the chamber freezes
 132 (before crystallinity reaches 50%), here plotted for a parent magma with 5 wt% H₂O initially at 200 MPa and critical
 133 overpressures of 20 MPa.
 134

135 This idealized model can explain, to a first order, trends in eruption frequency and
 136 volume for a number of long-lived volcanic systems ([Degruyter et al., 2016](#); [Degruyter, Huber,](#)
 137 [Bachmann, Cooper, & Kent, 2017](#); [Forni et al., 2018](#)). We first extend the model to account for
 138 the transition of magma between volatile undersaturation and volatile saturation/exsolution to
 139 form a magmatic volatile phase (MVP). We then use this framework to consider how the
 140 cooling, injection, and viscous relaxation timescales (τ_{cool} , τ_{in} , and τ_{relax}) influence the growth
 141 of the chamber and the proportion of magma that is erupted versus stored ($M_{er}:M_{add}$). The high
 142 compressibility of the MVP is expected to decrease the eruption frequency but increase the
 143 eruption size from shallow magma chambers ([Bower & Woods, 1997](#); [Caricchi, Annen, Blundy,](#)
 144 [Simpson, & Pinel, 2014](#); [Degruyter et al., 2016](#); [Huppert & Woods, 2002](#); [Woods & Huppert,](#)

145 [2003](#)); we explore how this competition ultimately impacts the long-term growth and stability of
146 the chamber.

147 The key timescales (τ_{cool} , τ_{in} , and τ_{relax}) and the magmatic volatile content can be
148 variably constrained at caldera systems by a combination of geologic, petrologic, and
149 geophysical data. In this paper, we begin by summarizing constraints on τ_{cool} , τ_{in} , and τ_{relax}
150 from inter-caldera eruptive episodes four silicic systems (Laguna del Maule, Campi Flegrei,
151 Santorini, and Aso), which we use to compare with the results of the thermo-mechanical model
152 for magma chamber growth. Based on these comparisons, we seek scaling relationships that can
153 be used to infer chamber growth and volatile exsolution from the eruptive history alone
154 (frequency and size distribution).

155

156 **2. Evolution of magma chambers in caldera systems**

157 Constraining the timescale for magma injection, $\tau_{in} = \frac{\rho V}{\dot{M}_{in}}$, requires an estimate for the
158 rate of magma supply \dot{M}_{in} to the chamber. In reality, magma likely is delivered in pulses as dikes
159 propagate into and feed the chamber. At active volcanoes, these events manifest as (1) episodes
160 of surface uplift as the underlying chamber inflates ([Le Mevel, Gregg, & Feigl, 2016](#); [Parks et al., 2012](#)), and (2) episodes of increased seismicity ([McKee et al., 1984](#); [Papadopoulos, Sachpazi, Panopoulou, & Stavrakakis, 1998](#)). The magnitude and distribution of vertical and horizontal
162 surface displacements are related to the depth, shape, and volume change of the chamber, which
163 are used to estimate the volumetric magma inflow rate. These rates typically are significantly
164 greater (order ~ 0.01 km³/yr) than long-term average magma supply rates (order ~ 0.001 km³/yr),
165 which are determined by other means; for example, the average rate of volcanic output can be
166 used to place a minimum bound on the long-term supply rates, and in some cases structural and
167 geomorphic data permit estimates of the volume added to the crust over geologic periods of time
168 ([Singer et al., 2018](#)). Thermally and mechanically, we expect little difference in the average
169 behavior (e.g. eruption frequency) of magma chambers subject to high-rate, short duration or
170 low-rate, long-duration recharges for a similar long-term average inflow rate ([Degruyter et al., 2016](#)). We therefore estimate long-term averaged values and use a constant mass inflow rate in
172 the model.
173

174 Geophysical data from seismic, gravity, and magnetotelluric surveys can provide
175 constraints on the present-day volume V of crustal chambers at active volcanoes ([Magee et al.,](#)
176 [2018](#)), which are required to estimate both τ_{in} and $\tau_{cool} = \frac{R^2}{\kappa}$. Petrologic data from eruptive
177 deposits constrain magma storage conditions such as pressure, temperature, and dissolved
178 volatile content, from which we can infer the presence of a magmatic volatile phase (MVP)
179 within chambers prior to eruptions.

180 An estimate of the crustal relaxation timescale $\tau_{relax} = \frac{\eta_r}{\Delta P_c}$ requires constraints on the
181 effective viscosity η_r of the host-rock surrounding the chamber, and the critical overpressure ΔP_c
182 required to initiate an eruption. Jellinek and DePaolo ([2003](#)) estimate ΔP_c required to propagate a
183 rhyolite dike to the surface and find that $\Delta P_c \sim 10 - 40$ MPa, based on scaling of the cooling rate
184 of the dike. Here we adopt a value of 20 MPa. Although host-rock viscosity can vary by a few
185 orders of magnitude depending on the lithology, temperature, and state of stress, we use a single
186 value for effective viscosity of 10^{19} Pa·s for each of the magmatic systems presented here,
187 resulting in $\tau_{relax} \sim 16$ ky. This value would be consistent with a chamber at ~ 7.5 km depth for a
188 normal geothermal gradient (30 °C/km), or shallower depths with more thermally mature crust
189 ([Karlstrom, Dufek, & Manga, 2010](#)). For the shallower volcanic systems presented here, greater
190 values of viscosity may be more appropriate. We note that since $\tau_{relax} \propto \eta_r$ the effects of greater
191 viscosity may be seen by shifting τ_{relax} and $\theta_2 = \frac{\tau_{relax}}{\tau_{in}}$ proportionally.

192

193 ***2.1 Laguna del Maule, Chile***

194 Laguna del Maule Volcanic Field is located ~ 80 km east of the active volcanic arc in the
195 southern Andes and currently is one of the best studied caldera systems in the world
196 (<http://geoscience.wisc.edu/rhyolitic/>). The system comprises ~ 350 km³ of lavas and tuffs of
197 basaltic to rhyolitic composition erupted throughout the Pleistocene ([Wes Hildreth, Godoy,](#)
198 [Fierstein, & Singer, 2010](#)). Evidence of at least two catastrophic caldera-forming eruptions
199 include a dacite ignimbrite aged ~ 1.5 Ma and a ~ 80 km³ biotite-rhyodacite tuff aged ~ 950 ka
200 ([Wes Hildreth et al., 2010](#); [Singer et al., 2014](#)). The last major large-volume eruption produced
201 ~ 20 km³ of rhyolitic tephra and coincides with deglaciation at ~ 25 ka ([Singer et al., 2014](#)). Since
202 this time, over 13 km³ of crystal-poor rhyolite ($<10\%$ phenocrysts) have erupted, and the

203 volcanic activity was concentrated into two phases: an early post-glacial period from ~25-19 ka
204 that output ~1.5 km³ from about 20 eruptions, and a Holocene phase from ~8 – 1.9 ka that output
205 >3.3 km³ from only about 10 eruptions ([Singer et al., 2014](#))(Table 1). Magma storage conditions
206 during these phases were relatively cold and wet; water contents dissolved in the melt range from
207 about 4.4 – 6.0 wt% for both rhyolites and rhyodacites ([Andersen et al., 2018](#)). Magnetite-
208 ilmenite thermometry from samples of both early post-glacial and Holocene eruptions suggests
209 temperatures of ~760 – 850 °C, and amphibole thermobarometry indicates pressures of ~180 –
210 250 MPa ([Andersen et al., 2017](#)). At these pressures, temperatures, and water contents, rhyolitic
211 magma likely is water-saturated.

212 Since 2007, a 200 km² area of the Laguna del Maule lake basin has been uplifting at a
213 rate of about ~25 cm/yr, inferred to be due to intrusion of magma to a sill-shaped body at ~5 km
214 depth at a rate of ~0.025 – 0.05 km³/yr ([Feigl et al., 2014](#); [Le Mevel et al., 2016](#)). The current
215 inflation is thought to exemplify one of several episodic magma recharge events that occurred
216 throughout the Holocene, accumulating in over 60 meters of uplift since 9.4 ka and supplying
217 ~13 km³ of magma, indicating a long-term average recharge rate of 0.0023 km³/yr ([Singer et al.,](#)
218 [2018](#)). A gravity anomaly ~2 – 4 km beneath the lake is interpreted as a low-density (1800 –
219 1900 kg/m³), crystal-poor (< 50%), and volatile-rich zone about 30 km³ in volume embedded
220 within a larger (>100 km³) zone of crystal rich (> 70%) cumulate mush ([C. A. Miller, Williams-](#)
221 [Jones, Fournier, & Witter, 2017](#)). The ratio of magma erupted (~8.4 km³) to the volume of
222 magma added (~13 km³) during the last ~9.4 ka suggests that magma injection has led to
223 reservoir growth throughout the Holocene and possibly since the last major plinian eruption of
224 the Rhyolite of Laguna del Maule (*rdm*) at ~25 ka. Using a chamber volume of ~ 30 km³ from
225 the gravity data ([C. A. Miller et al., 2017](#)), and the long-term magma supply rate (0.0023 km³
226 /yr), the injection timescale $\tau_{in} \sim 13$ ky and the cooling timescale $\tau_{cool} \sim 117$ ky. Prior to the
227 Holocene phase, when the chamber was likely smaller by >13 km³, these timescales would have
228 been closer to $\tau_{in} \sim 7.5$ ky and $\tau_{cool} \sim 79$ ky (Table 1).

229

230 **2.2 Campi Flegrei, Italy**

231 Campi Flegrei, located a few kilometers west of Naples and home to over 1.5 million
232 people, consists of two nested calderas associated with the ~300 km³ eruption of the Campanian

233 Ignimbrite (CI) at ~39 ka and the ~40 km³ Neapolitan Yellow Tuff (NYT) at ~15 ka ([Deino,](#)
234 [Orsi, de Vita, & Piochi, 2004](#)). Since the NYT, about 60 more eruptions have occurred ranging
235 in composition from basaltic trachy-andesite to trachy-phonolite, arriving in three epochs of
236 activity ([Bevilacqua, Flandoli, Neri, Isaia, & Vitale, 2016](#); [Di Vito et al., 1999](#); [Orsi, Di Vito, &](#)
237 [Isaia, 2004](#); [Smith, Isaia, & Pearce, 2011](#)): The first epoch was from ~15.0 – 9.5 ka and included
238 about 34 explosive eruptions totaling ~5.4 km³; the second epoch was the shortest, lasting from
239 ~8.6 – 8.2 ka with 6 explosive eruptions totaling ~0.69 km³ ([Smith et al., 2011](#)); the third epoch
240 from ~4.8 – 3.8 ka included 16 explosive eruptions and 4 effusive eruptions totaling ~2.5 km³
241 ([Smith et al., 2011](#)) (Table 1). Following the CI eruption at ~39ka, magma storage conditions
242 were relatively hot (1000-1090 °C), dry (3-5 wt% water), and mafic, evolving to colder (880-930
243 °C) and wetter conditions (5-7 wt% water) just prior to the eruption of the NYT ([Forni et al.,](#)
244 [2018](#)). After the NYT, the reservoir become once again hot, dry, and mafic (1070-1130 °C with
245 0.2 – 3.5 wt% water), progressing to colder and wetter conditions throughout the 1st, 2nd, and 3rd
246 epochs (900-1080 °C and 3-6 wt%) ([Forni et al., 2018](#); [M. Stock et al., 2018](#)). The most recent
247 eruption of Monte Nuovo in 1538 continued on this trend (870-920 °C and 5-7 wt%) ([Forni et](#)
248 [al., 2018](#)).

249 The minimum magma supply rates for the three epochs constrained from eruptive
250 volumes are ~0.001 km³/yr, ~0.0017 km³/yr, and ~0.0025 km³/yr, respectively. A maximum
251 bound on magma supply rate is found by considering an individual recharge event; for example,
252 using the estimate of Di Vito et al. ([2016](#)) for a volume change of ~0.93 to 0.95 km³ over the
253 period 1400-1536 AD gives a magma recharge rate of ~0.007 km³/yr. To estimate the injection
254 timescale for the Campi Flegrei magma chamber, we use an intermediate estimate for the long-
255 term magma supply rate of ~0.003 km³/yr. Geophysical surveys indicate the presence of a
256 shallow magmatic body, although the volume and distribution of melt is not well constrained
257 ([Calo & Tramelli, 2018](#); [Fedi et al., 2018](#); [Zollo et al., 2008](#)). Recent modeling by Forni et al.
258 ([2018](#)) find a good match between the predicted and estimated cumulative eruptive volumes for
259 each of the three epochs by using an initial magma chamber volume of ~2.5 km³ that grows to
260 ~11 km³ by the end of the third epoch. Using these estimates for chamber volume and magma
261 supply rates, we estimate that τ_{in} would have increased from ~0.8 ky during the first epoch to
262 ~3.5 ky during the third epoch. τ_{cool} would have increased from ~22.5 to ~60 ky (Table 1).

263

264 *2.3 Santorini, Greece*

265 Santorini (Thera) is a large volcanic complex within the Hellenic subduction zone, where
266 explosive volcanic activity began at least ~360 ka ([Druitt, Mellors, Pyle, & Sparks, 1989](#)).
267 Multiple, nested calderas and well-exposed volcanic stratigraphy indicate that the volcano cycles
268 between large, explosive Plinian-style eruptions and smaller, effusive shield-building eruptions
269 ([Druitt & Francaviglia, 1992](#)). The oldest caldera dates back to ~180 ka, followed by the Skaros
270 caldera at ~70 ka, the Cape Riva caldera at ~21 ka, and the caldera associated with the Late-
271 Bronze-Age (Minoan) eruption ~3600 years ago that ejected ~40 – 80 km³ DRE and devastated
272 Minoan settlements on the island ([Druitt & Francaviglia, 1992](#); [Johnston, Sparks, Phillips, &](#)
273 [Carey, 2014](#); [Sigurdsson et al., 2011](#)). Since the Minoan eruption, at least 11 eruptions have
274 occurred, giving an average eruption frequency of ~3 ky⁻¹ ([Pyle & Elliott, 2006](#)). These eruptions
275 have been dominantly effusive lavas that built up the Kameni islands in the center of the caldera
276 bay, and have ranged in volume from ~0.0006 – 0.14 km³, with the volume varying in proportion
277 with the repose time ([Parks et al., 2012](#)). Deposits from the four major caldera-forming eruptions
278 indicate relatively cold and wet conditions (850 – 900 °C and 2 – 7 wt% H₂O) compared to the
279 post-caldera lavas (960 – 1012 °C and 1-4 wt% H₂O) ([Barton & Huijsmans, 1986](#); [Cadoux,](#)
280 [Scaillet, Druitt, & Deloule, 2014](#); [Cottrell, Gardner, & Rutherford, 1999](#); [Druitt et al., 2016](#)).
281 Petrologic data combined with modeling by Degruyter et al. ([2016](#)) suggest that the magma
282 chamber was water saturated prior to the Minoan eruption, but has been drier and possibly even
283 undersaturated ever since.

284 The volume of the Minoan eruption ~3600 ka indicates that the chamber grew to volumes
285 of ~40 – 80 km³ over ~18 ky since the previous caldera-forming eruption, implying a long-term
286 average magma supply rate of ~0.002 – 0.004 km³/yr. However, approximately 7-15% of the
287 erupted material is thought to be magma that recharged the system ~10-100 years prior ([Druitt,](#)
288 [Costa, Deloule, Dungan, & Scaillet, 2012](#); [Flaherty et al., 2018](#)), which would imply a more
289 episodic recharge at a rate of ~0.05 km³/yr. Episodic recharge also is supported by the recent
290 inflation and seismic unrest in 2011-2012, which suggested the arrival of ~0.01 km³ of magma to
291 a chamber at ~3 – 6 km depth ([Parks et al., 2012](#)), giving a recharge rate of ~0.01 km³/yr.
292 Throughout post-Minoan times, the background average magma recharge rate has been ~0.001
293 km³/yr, estimated from the volume of the dome in the caldera bay constructed since the Minoan

294 eruption ($\sim 2.5 \text{ km}^3$) and the volume of material erupted since AD 1570 ([Parks et al., 2012](#)). The
295 small volumes and high frequencies of post-Minoan lavas suggests that the chamber was
296 substantially smaller than it was prior to the Minoan eruption; the model by Degruyter et al.
297 ([2016](#)) shows a good fit to eruptive volumes using a model chamber $\sim 10 \text{ km}^3$ in volume
298 containing no exsolved volatiles. Using this volume and the estimated long-term magma supply
299 during the post-caldera period ($0.001 \text{ km}^3/\text{yr}$), we estimate $\tau_{in} \sim 10 \text{ ky}$ and $\tau_{cool} \sim 57 \text{ ky}$. Prior to
300 the Minoan eruption, using a chamber volume of $\sim 50 \text{ km}^3$ and the long-term magma supply since
301 the Cape Riva ($\sim 0.0028 \text{ km}^3/\text{yr}$), we estimate $\tau_{in} \sim 18 \text{ ky}$ and $\tau_{cool} \sim 165 \text{ ky}$ (Table 1).

302

303 **2.4 Aso, Japan**

304 The large volcanic complex of Aso, in Kyushu, southern Japan, has had at least four
305 major caldera-forming eruptions: Aso-1 at 266 ka ($\sim 50 \text{ km}^3$), Aso-2 at 141 ka ($\sim 50 \text{ km}^3$), Aso-3
306 at 123 ka ($> 150 \text{ km}^3$), and Aso-4 at 90 ka ($> 600 \text{ km}^3$) ([Kaneko et al., 2007](#)). The extraordinary
307 size of the two most recent caldera-forming eruptions (Aso-3 and Aso-4) suggests that the
308 underlying magma chamber is capable of growing to several hundred cubic kilometers in volume
309 in the span of a few tens of thousands of years. Since Aso-4 at 90 ka, eruptive activity has
310 continued and is concentrated into two pulses: Phase 1 from $\sim 70 - 50 \text{ ka}$, consisting of 18 tephra
311 units totaling $\sim 5 \text{ km}^3$, and 6 lava units totaling $\sim 1 \text{ km}^3$; and Phase 2 from $\sim 40 - 20 \text{ ka}$ consisting
312 of 6 tephra units totaling $\sim 3 \text{ km}^3$, and 8 lava units totaling $\sim 1.3 \text{ km}^3$ ([Miyabuchi, 2009](#); [Miyoshi
313 et al., 2012](#)). Altogether, the eruption frequency from Phase 1 ($\sim 1.2 \text{ ky}^{-1}$) is almost double that of
314 Phase 2 ($\sim 0.7 \text{ ky}^{-1}$) while the average eruption volume is slightly greater during Phase 2 (~ 0.29
315 km^3 per eruption) compared to Phase 1 ($\sim 0.25 \text{ km}^3$ per eruption) (Table 1).

316 From the volume of post-caldera cone edifices (112 km^3) that were built over the last 90
317 ky, the magma supply rate at Aso is estimated to be $\sim 0.0015 \text{ km}^3/\text{yr}$ ([Miyabuchi, 2009](#)). A recent
318 3D electrical resistivity study imaged what is interpreted to be the shallow crustal reservoir, with
319 a roof located at $\sim 6 \text{ km}$ depth ([Hata et al., 2018](#)), in agreement with seismic data ([Sudo & Kong,
320 2001](#)). The resistivity data are interpreted as showing a magma body $\sim 6.3 \text{ km}^3$ in volume with
321 melt fractions of 96-99%, contained within a mush zone $\sim 90 \text{ km}^3$ with lower melt fractions (2-
322 3%) ([Hata et al., 2018](#)). Without further constraints on historical chamber volumes over the last

323 90 ky, we use the present-day constraint of 6.3 km³ to estimate $\tau_{in} \sim 4.1$ ky and $\tau_{cool} \sim 41$ ky
 324 (Table 1).

325

Volcano, epoch	Eruption frequency (ky ⁻¹)	Average eruption volume (km ³)	Caldera cycle (ky)	Chamber volume (km ³)	Magma supply (km ³ /yr)	τ_{in} (ky)	τ_{cool} (ky)
LdM, EPG	5.5*	0.046*	550-925 [§]	$\sim 17^{\ddagger\#}$	0.0023 [†]	7.5	79
LdM, Holocene	1*	0.55*	550-925 [§]	$\sim 30^{\wedge}$	0.0023 [†]	13	117
CF Epoch 1	6.2 [†]	0.16 [†]	$\sim 24^{\dagger}$	$\sim 2.5^{\bullet}$	0.003 [†]	0.8	22.5
CF Epoch 2	15 [†]	0.11 [†]	$\sim 24^{\dagger}$	$\sim 7^{\bullet}$	0.003 [†]	2.3	44
CF Epoch 3	16 [†]	0.16 [†]	$\sim 24^{\dagger}$	$\sim 11^{\bullet}$	0.003 [†]	3.5	60
Santorini, post-Minoan	3 ⁻	0.064 ⁻	18 to 110 ⁻	$\sim 10^{\cdot}$	0.001 ⁻	10	57
Santorini, pre-Minoan	--	--	18 to 110 ⁻	$\sim 50^{\&}$	0.0028 ^{&}	18	165
Aso Phase 1	1.2 [‡]	0.25 [‡]	18 to 125 ⁺	$\sim 6.3^{\!}$	0.0015	4.1	41
Aso Phase 2	0.7 [‡]	0.29 [‡]	18 to 125 ⁺	$\sim 6.3^{\!}$	0.0015	4.1	41

326 **Table 1.** Summary of constraints on eruption frequency, volume, caldera cycle length, and the timescales for
 327 injection and cooling during various eruptive phases at four different large silicic systems. LdM = Laguna del
 328 Maule; EPG = Early Post-Glacial period; CF = Campi Flegrei *[\(Singer et al., 2014\)](#) #[\(Singer et al., 2018\)](#) ^[\(C. A. Miller et al., 2017\)](#) §[\(Wes Hildreth et al., 2010\)](#) †[\(Smith et al., 2011\)](#) †[\(Forni et al., 2018\)](#) -[\(Parks et al., 2012\)](#)
 329 &[\(Johnston et al., 2014\)](#) †[\(Degruyter et al., 2016\)](#) ‡[\(Miyabuchi, 2009\)](#) †[\(Kaneko et al., 2007\)](#) †[\(Hata, Takakura, Matsushima, Hashimoto, & Utsugi, 2016\)](#)
 330
 331

332

333 3. Modeling eruption frequency, volume, and chamber growth

334 In this section, we present modeling results for eruption frequency and chamber growth
 335 as a function of the fundamental timescales τ_{in} , τ_{cool} , and τ_{relax} , as well as the initial water
 336 content of the magma X_{H_2O} . In this way, we can compare the eruptive history at Laguna del
 337 Maule, Campi Flegrei, Santorini, and Aso to the output of the model in order to better understand
 338 the long-term evolution and growth rates of these silicic magma chambers. Furthermore, we aim
 339 to gain a broader understanding of the conditions that promote growth, and we test whether we
 340 can use changes in the frequency and size of volcanic eruptions to determine changes in the size
 341 and volatile saturation state of the underlying chamber.

342 *3.1 Model setup and model parameters*

343 The magma chamber model of Degruyter and Huber (2014) approximates the chamber as
344 a sphere of radius R and volume V containing a mixture of silicate melt, solid crystals, and a
345 magmatic volatile phase (MVP), here assumed to be water. We assume the chamber is spatially
346 homogeneous and calculate average values of pressure, temperature, density, and crystal and
347 MVP volume fractions. Magma recharge is a constant mass inflow rate \dot{M}_{in} at a specified
348 temperature and initial dissolved water content X_{H_2O} . Recharge adds mass and energy to the
349 chamber, while the chamber simultaneously loses heat to the surroundings. We envision the
350 surrounding crust as a transition from a crystal-rich mush near the chamber (>50% crystals) to
351 fully-solid crust farther away; therefore, we model the rheology as viscoelastic similar to other
352 treatments (Del Negro, Currenti, & Scandura, 2009; Dragoni & Magnanensi, 1989; Newman,
353 Dixon, & Gourmelen, 2006; Segall, 2016) but calculate an effective viscosity η_r from a viscosity
354 gradient that depends on the temperature profile of the crust around the chamber. Conservation
355 of mass, water, and energy are combined with closure equations for crystallinity, water
356 solubility, and gas density. The melting curve implemented here uses a parameterization by
357 (Huber, Bachmann, & Manga, 2009) for a dacite composition, and the solubility law comes from
358 the parameterization of Dufek and Bergantz (2005) based on Zhang (1999) for solubility of water
359 in rhyolite.

360 When the pressure reaches a specified critical value $P_{lit} + \Delta P_c$, an “eruption” occurs and
361 mass is extracted from the chamber at a constant rate \dot{M}_{out} (here fixed to 10^5 kg/s) until the
362 pressure returns to the lithostatic value, here set to $P_{lit} = 200$ MPa. The model simulation ends
363 when the crystal volume fraction reaches 50%, at which point we assume the magma is immobile
364 and unlikely to erupt again.

365 The model has been extended to account for transitions between volatile saturation,
366 accompanied by exsolution of gas, and undersaturation. We assume that water is the only volatile
367 phase and that it is perfectly incompatible, so that as crystallization proceeds, all of the water
368 remains in the melt and the concentration increases. The initial mass fraction of water in the melt
369 within the chamber is set to $X_0^r = \frac{X_{H_2O}}{\epsilon_{m,0}}$ where X_{H_2O} is the total mass fraction of water in the
370 parent magma and $\epsilon_{m,0}$ is the initial volume fraction of melt in the chamber. The concentration
371 of water in the melt is tracked in time as crystallization increases the concentration, as recharge

372 adds melt at a specified concentration (here the same as the parent melt, X_{H2O}), and as eruptions
 373 remove melt at a concentration assumed to be that of the melt in the chamber X' . When X' is less
 374 than the water solubility m_{eq} , only two conservation equations are solved (total mass and energy);
 375 when X' exceeds the water solubility m_{eq} , the gas volume fraction is solved for using an
 376 additional equation governing conservation of water mass.

377 Table 2 provides the initial conditions and range of model parameters . We use the model
 378 results to calculate the average eruption frequency f as a function of the mass recharge rate,
 379 initial chamber mass and volume, mass fraction of water, and host-rock effective viscosity, as we
 380 formulate this in terms of the three fundamental timescales τ_{in} , τ_{cool} , and τ_{relax} . In addition, we
 381 calculate the total mass and volume of magma erupted, summing over all of the eruptions over
 382 the course of the simulations (i.e. until $\epsilon_x = 50\%$). We compare this to the amount of mass and
 383 volume added to the system by recharge, in order to understand how the growth of the chamber
 384 by mass and volume is influenced by the three timescales and water content. Finally, we use the
 385 model results to calculate growth rates as a function of τ_{in} , τ_{cool} , and τ_{relax} , to be compared
 386 with the growth rates and caldera cycle periods estimated for the four volcanic systems discussed
 387 in Section 2.

388

Parameter	Definition	Range of values used
$V_0 = \frac{4}{3}\pi R_0^3$	Initial chamber volume (km ³)	0.0005 – 500 km ³
\dot{M}_{in}	Mass inflow rate (kg/s)	0.1 – 500 kg/s ($\sim 10^{-6} - 6 \cdot 10^{-3}$ km ³ /yr)
X_{H2O}	Water concentration of parent magma	3 – 7 wt%
P_{lit}	Ambient pressure (lithostatic)	200 MPa
ΔP_c	Critical overpressure	20 MPa
T_0	Initial chamber temperature	1200 K
T_b	Temperature at edge of viscoelastic shell (far-field temperature)	500 K

S	Radius of viscoelastic shell	$10 \cdot R_0$
κ	Thermal diffusivity of crust	$10^{-6} \text{ m}^2/\text{s}$
$\rho_{m,0}$	Initial density of melt	2400 kg/m^3
$\rho_{x,0}$	Initial density of crystals	2750 kg/m^3
$\beta_m, \beta_x, \beta_r$	Compressibility of melt, crystals, and host rock	10^{-10} Pa^{-1}
θ_1	$\frac{\tau_{cool}}{\tau_{in}} = \frac{3}{4\pi} \frac{\dot{M}_{in}}{\kappa \rho_0 R_0}$	$10^{-3} - 10^3$
θ_2	$\frac{\tau_{relax}}{\tau_{in}} = \frac{3}{4\pi} \frac{\dot{M}_{in} \eta_{r,0}}{\Delta P_c \rho_0 R_0^3}$	$10^{-3} - 10^3$

Table 2. Values for the model parameters used to calculate eruption frequencies, volumes, and growth rates

3.2 Modeling results

3.2.1 Eruption frequency and volume

For a given chamber volume, the average eruption frequency increases with greater magma recharge rates (Figure 2a). However, the water content of the parent magma also affects eruption frequency. In the example shown in Figure 2a, the eruption frequency is plotted against magma recharge rate for a chamber with an initial volume of 5 km^3 and three different initial water contents: a dry case (3 wt%) an intermediate case (5 wt%), and a wet case (7 wt%). For the dry case, none of the simulations reach volatile saturation to form a magmatic volatile phase (MVP); in contrast, the wet case always reaches saturation and exsolves volatiles. While all of the simulations show increasing eruption frequency with magma recharge rate, the simulations with 3 wt% water resulted in frequencies that were greater by a factor of ~ 5 - 6 compared to the models with 7 wt% water. For the intermediate case, at magma recharge rates less than about $0.5 \times 10^{-3} \text{ km}^3/\text{yr}$, eruption frequencies are similar to those for the wet case. However, once magma recharge increases to about $10^{-3} \text{ km}^3/\text{yr}$, the eruption frequency increases abruptly such that by $M_{in} \sim 1.3 \times 10^{-3} \text{ km}^3/\text{yr}$ the intermediate case behaves identically to the dry case.

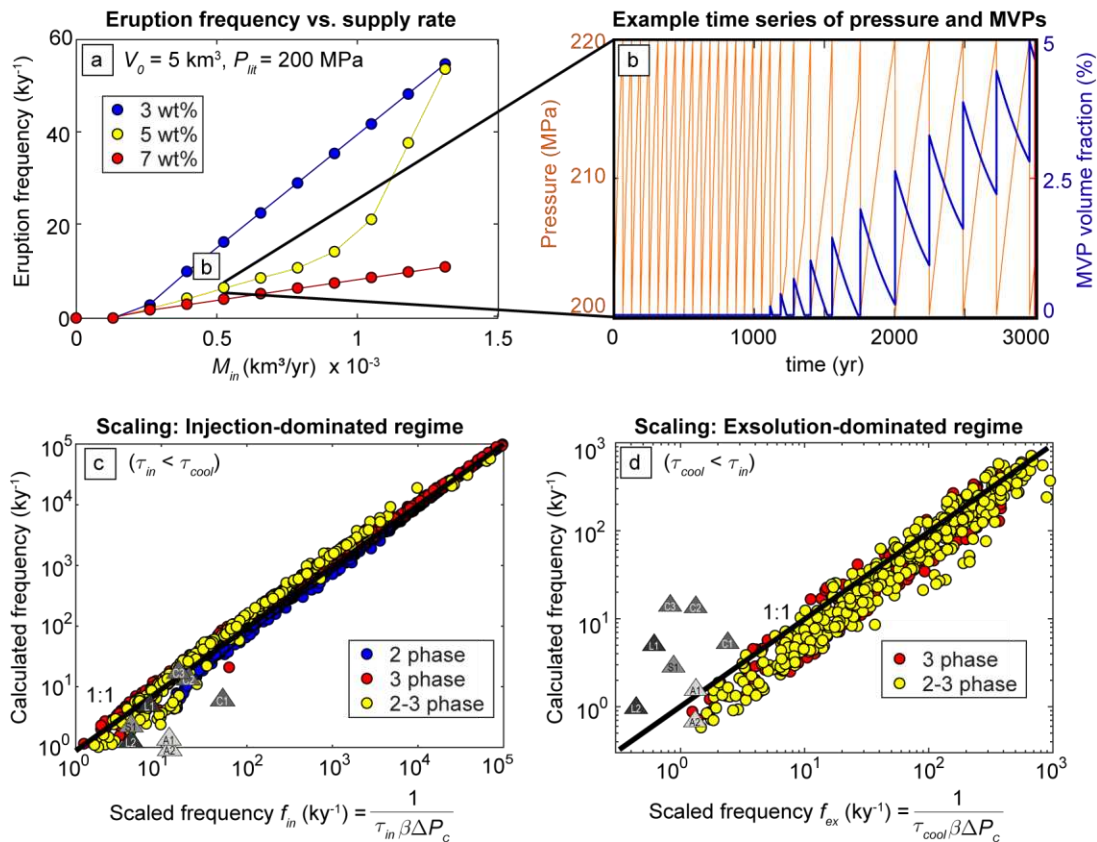
This behavior is linked to the evolution of the MVP volume fraction ϵ_g and its effect on the bulk magma compressibility β :

$$\beta = \frac{1}{\rho} \left(\epsilon_m \rho_m \beta_m + \epsilon_x \rho_x \beta_x + \epsilon_g \frac{\partial \rho_g}{\partial P} \right) \quad (4)$$

408

409 For example, in the case of 3 wt% water and $M_{in} \sim 0.5 \times 10^{-3} \text{ km}^3/\text{yr}$, the magma never reaches
 410 volatile saturation ($\epsilon_g = 0$) and the mixture remains two-phase (crystals + melt) with a consistent
 411 eruption frequency of about 18 ky^{-1} throughout its lifespan. In the case with 5 wt% water, the
 412 magma is initially MVP-free but after about 1000 years becomes saturated and exsolves an MVP
 413 (Figure 2b). Exsolution of the MVP corresponds to a sharp decrease in the eruption frequency,
 414 dropping from $\sim 18 \text{ ky}^{-1}$ to $\sim 4 \text{ ky}^{-1}$ (Figure 2b). In the wet case, the magma is initially saturated
 415 and the MVP continues to exsolve throughout the simulation, and the eruption frequency is
 416 consistently about 4 ky^{-1} .

417



418

419 **Figure 2.** (a) Average eruption frequency (in ky^{-1}) as a function of magma recharge rate (km^3/yr) for three different
 420 initial water concentrations. Model labeled b is shown in detail in the right-hand panel (b) Evolution of chamber
 421 pressure and gas volume fraction in time for an initially slightly undersaturated magma (5 wt%). (c) Average
 422 eruption frequency (ky^{-1}) as a function of the inverse of the injection timescale, bulk compressibility, and critical
 423 overpressure. Dots are colored according to the number of phases present throughout the model simulation (2 = melt
 424 and crystals only; 3 = melt, crystals, and gas only; 2-3 = transition between two and three phases) (d) Average

425 eruption frequency as a function of the inverse of the cooling timescale, compressibility, and critical overpressure.
 426 Shaded triangles represent the volcanic systems of Laguna del Maule (L1 = Early post-glacial period; L2 =
 427 Holocene), Campi Flegrei (C1 = 1st epoch, C2 = 2nd epoch, C3 = 3rd epoch), Santorini (S1 = post-Minoan period, S2
 428 = pre-Minoan), and Aso (A1 = Phase 1, and A2 = Phase 2). We use values of $\beta \sim 10^{-9} \text{ Pa}^{-1}$ and $\Delta P_c \sim 20 \text{ MPa}$ for the
 429 volcanic systems.

430

431 We provide scaling relationships for eruption frequency that consider the combined
 432 effects of the mass recharge rate, initial chamber volume, and the average magma
 433 compressibility β . When mass recharge dominates the evolution of pressure ($\tau_{in} < \tau_{cool}$, Region
 434 2 of Fig. 1), the eruption frequency f_{in} is inversely proportional to the injection timescale, the
 435 average bulk compressibility of the magma β , and the critical overpressure ΔP_c . When exsolution
 436 dominates the evolution of pressure ($\tau_{cool} < \tau_{in}$, Region 1 of Fig. 1), the eruption frequency f_{ex}
 437 is inversely proportional to the cooling timescale, β , and ΔP_c :

438

$$439 \quad f_{in} = \frac{1}{\tau_{in}\beta\Delta P_c} \quad (\tau_{in} < \tau_{cool}) \quad (5)$$

440

$$441 \quad f_{ex} = \frac{1}{\tau_{cool}\beta\Delta P_c} \quad (\tau_{in} > \tau_{cool}) \quad (6)$$

442

443 These scaling relationships are a good approximation of the model results (Fig. 2c and d). In
 444 addition, the trends in eruption frequencies for the various phases of volcanic activity at
 445 Santorini, Laguna del Maule, and Campi Flegrei are predicted moderately well by the scaling for
 446 the injection-dominated regime (Figure 2c). Aso Volcano is the only example that may be a
 447 better match to the scaling for eruptions triggered by second boiling (Figure 2d). On the other
 448 hand, uncertainties in estimated parameters or the assumption of identical β (10^{-9} Pa^{-1}) and ΔP_c
 449 (20 MPa) may cause a mismatch between scaling and observations. For example, if Aso Volcano
 450 has a greater volume fraction of MVPs than the other systems, β might be greater, shifting Aso
 451 left and closer to the scaling law for the injection-triggered regime.

452 Huppert and Woods (2002) provide a scaling relationship for the volume of a single
 453 eruption:

454

455 $V_{er} = V\beta\Delta P_c$ (7)

456

457 The good agreement between this scaling, the model results, and the eruption volume at silicic
 458 volcanic systems (Fig. 3) supports the validity of applying both the model and scaling to real
 459 systems. One useful application of these scaling laws is that we can potentially constrain the size
 460 and volatile saturation state of a magma chamber from the changes in eruption history. For
 461 example, consider the two eruptive phases of Laguna del Maule, the early post-glacial (E) and
 462 Holocene phases (H). During the early post-glacial phase, the eruption frequency was about 5.5
 463 times greater and the eruptive volume was about 1/10 of what it was during the Holocene (Table
 464 1). From the scaling for eruption frequency (eq. 5) and volume (eq. 7), and assuming the critical
 465 overpressure is unchanged, this implies:

466
$$\frac{f_{in,E}}{f_{in,H}} \sim \frac{\tau_{in,H} \beta_H}{\tau_{in,E} \beta_E} \sim \frac{\dot{M}_{in,E} V_H \beta_H}{\dot{M}_{in,H} V_E \beta_E} \sim 5.5$$
 (8)

467

468
$$\frac{V_{er,E}}{V_{er,H}} \sim \frac{V_E \beta_E}{V_H \beta_H} \sim 0.1$$
 (9)

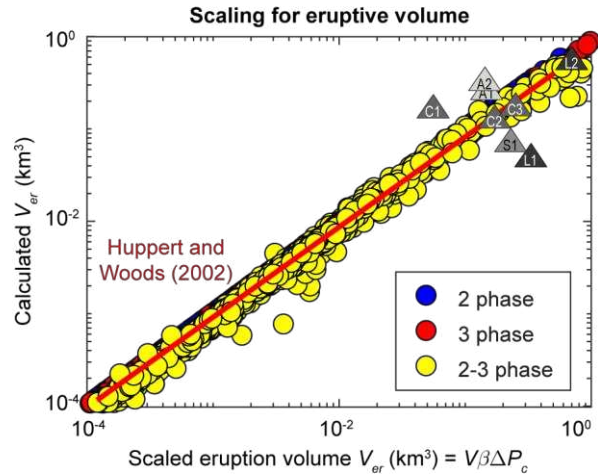
469

470 Substituting eq. (9) into eq. (8), we have

471
$$\frac{\dot{M}_{in,E}}{\dot{M}_{in,H}} \sim 0.55$$
 (10)

472

473 These relationships can be satisfied if the magma chamber during the Holocene was larger and
 474 more compressible than it was during the early post-glacial period, all of which would be true if
 475 the chamber grew and exsolved volatiles during the last ~25 ky. For example, if the exsolution of
 476 volatiles led to an increase in the compressibility by a factor of 5, the volume of the chamber
 477 must have grown by a factor of ~2.



478

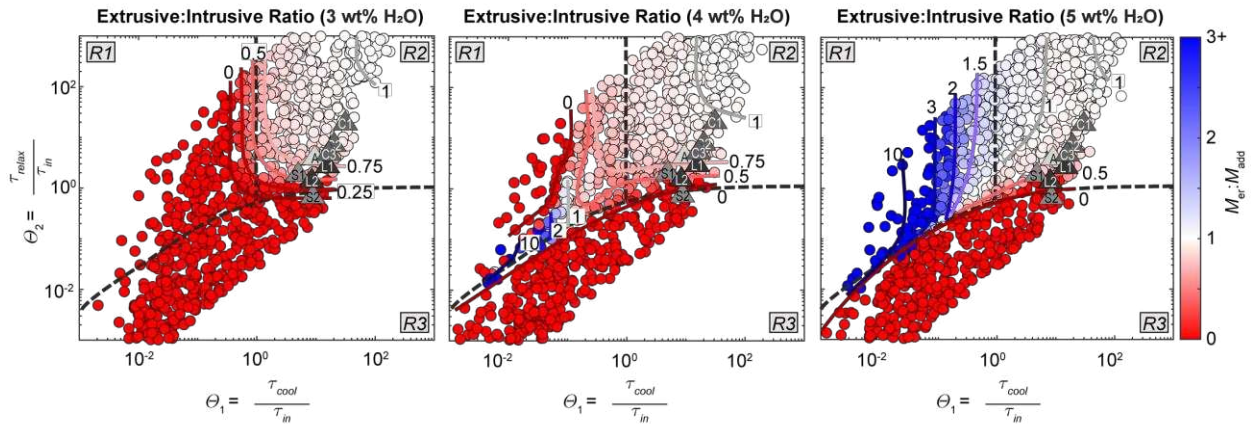
479 **Figure 3.** Average eruptive volume (per eruption) as a function of chamber volume V , compressibility β , and critical
 480 overpressure ΔP_c . Dots are colored according to the number of phases present throughout the model simulation (2 =
 481 melt and crystals only; 3 = melt, crystals, and gas only; 2-3 = transition between two and three phases). Red line
 482 represents the scaling for eruption volume (eq. 7) of Huppert and Woods (2002). Shaded triangles represent the
 483 volcanic systems of Laguna del Maule (L1 = Early post-glacial period; L2 = Holocene), Campi Flegrei (C1 = 1st
 484 epoch, C2 = 2nd epoch, C3 = 3rd epoch), Santorini (S1 = post-caldera period, S2 = pre-Minoan), and Aso (A1 =
 485 Phase 1, and A2 = Phase 2).

486

487 3.2.2 Ratio of mass erupted to mass added ($M_{er}:M_{add}$) and chamber growth

488 We calculate the total mass of magma erupted (summing over all eruptions) and supplied
 489 by recharge throughout the span of the model simulations (until crystal volume fraction reaches
 490 50%). The balance between mass erupted / mass added ($M_{er}:M_{add}$; a rough proxy for the
 491 extrusive:intrusive ratio) provides insight on the overall growth of the magma chamber. Model
 492 results for $M_{er}:M_{add}$ are plotted on regime diagrams for three different water concentrations
 493 (Figure 4). In the dry case (3 wt% water), almost none of the mass supplied by recharge is
 494 erupted, except within the injection-dominated regime (Region 2). Within this regime, $M_{er}:M_{add}$
 495 increases up and to the right, as the injection timescale decreases relative to the cooling and
 496 viscous relaxation timescales. In the wet case (5 wt% water), Regions 2 and 3 show a similar
 497 behavior to the dry case, with no eruptions occurring in Region 3 and so none of the mass
 498 leaving the chamber. However, the increased water content allows the possibility for eruption
 499 triggering by second boiling (Region 1). Within Region 1, we see that $M_{er}:M_{add} > 1$, indicating
 500 that there is significantly greater mass withdrawal during eruptions in this regime, such that
 501 magma chambers over time may actually shrink by mass. In Region 2, even though eruptions are

502 generally triggered by mass injection, we continue to see greater $M_{er}:M_{add}$ for the wet case. In the
 503 intermediate case (4 wt% water), $M_{er}:M_{add}$ is generally less than one across all regions, except for
 504 a few cases within Region 1 where eruptions are triggered by second boiling and significantly
 505 more mass is erupted than added. In Region 2, although $M_{er}:M_{add}$ increases to the top-right as it
 506 does in the dry case, the values are overall intermediate between the dry and wet case (Figure 4).



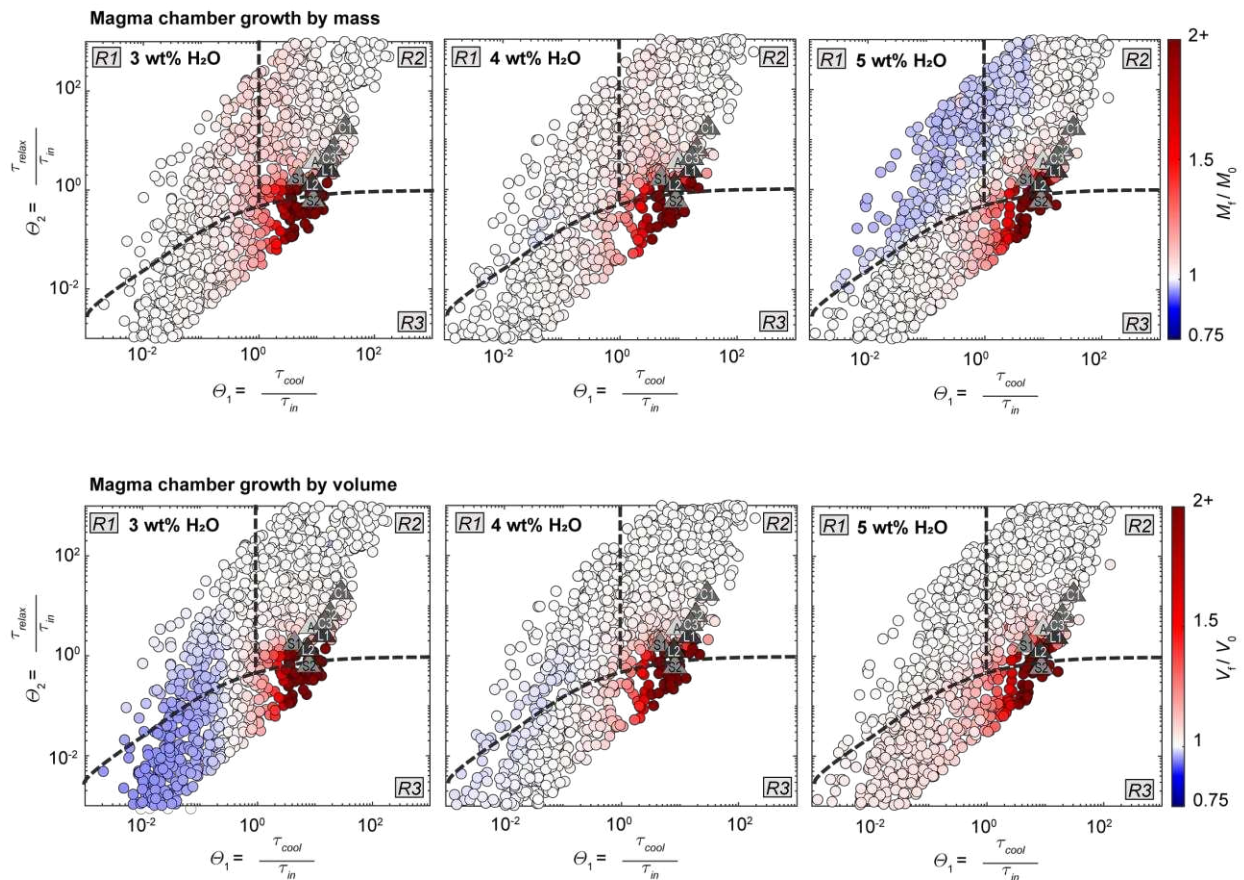
507
 508 **Figure 4.** Ratio of the total mass erupted to added (by recharge), once the magma chamber reaches 50% crystal
 509 volume fraction, plotted for three different initial water concentrations. Red indicates growth, blue indicates
 510 shrinkage. Shaded triangles represent the volcanic systems of Laguna del Maule (L1 = Early post-glacial period; L2
 511 = Holocene), Campi Flegrei (C1 = 1st epoch, C2 = 2nd epoch, C3 = 3rd epoch), Santorini (S1 = post-Minoan period,
 512 S2 = pre-Minoan), and Aso (A1 = Phase 1, and A2 = Phase 2).

513

514 While the extrusive:intrusive ratio $M_{er}:M_{add}$ is famously difficult to quantify in real
 515 systems, it is generally believed to vary between $\sim 0.1 - 0.5$ (White et al., 2006) for upper crustal
 516 systems. Using values for θ_1 and θ_2 estimated for Laguna del Maule, Santorini, Campi Flegrei,
 517 and Aso, we see that all of these systems are expected to have $M_{er}:M_{add} < 1$. Of the systems we
 518 consider here, Laguna del Maule currently is the best constrained in terms of $M_{er}:M_{add}$, with an
 519 estimated $\sim 8.4 \text{ km}^3$ erupted and 21.4 km^3 added (including erupted volume) over the Holocene,
 520 for a ratio of $M_{er}:M_{add} = 0.4$, which matches well with the predictions shown in Figure 4. In the
 521 regime space where the volcanic systems plot, $M_{er}:M_{add}$ appears to be most sensitive to the value
 522 of θ_2 , and does not appear to be very sensitive to water content (Fig. 4).

523 The overall effect on chamber growth of $M_{er}:M_{add}$ can be viewed in terms of the change in
 524 mass and volume of the chamber (M_f/M_0 and V_f/V_0). In Figure 5, we show M_f/M_0 and V_f/V_0 on the
 525 regime diagrams for the wet, intermediate, and dry cases. In all three cases, growth by both mass
 526 and volume is enhanced to the bottom-right of the regime diagrams, where θ_1 is large while θ_2 is

527 small. This “zone of efficient growth” occurs where greater mass recharge leads to short
 528 injection timescales, but where the relaxation timescale is comparable to the injection timescale,
 529 allowing growth by crustal deformation. This zone straddles the boundary between Region 2, in
 530 which many eruptions take place (Fig. 1), and Region 3, in which no eruptions take place (Fig.1).
 531 In other words, the model results indicate that growth can occur with or without eruptions. Using
 532 values for θ_1 and θ_2 estimated for Laguna del Maule, Santorini, Campi Flegrei, and Aso, we find
 533 that almost all of the volcanic systems fall within the “zone of efficient growth” overlapping
 534 Region 2, where eruptions occur and are dominated by injection (Fig. 5). Only the values for
 535 Santorini prior to the Minoan eruption fall within Region 3, but close to the boundary with
 536 Region 2. For all of these systems, model results predict growth by both mass and volume during
 537 eruptive phases, as seems to be occurring in nature.



538

539 **Figure 5.** Chamber growth by mass M_f / M_0 (upper panels) and volume V_f / V_0 (lower panels), for three different
 540 parental water concentrations. Red indicates growth, while blue indicates shrinkage. Shaded triangles represent
 541 volcanic phases from Laguna del Maule (L1 = Early post-glacial period; L2 = Holocene), Campi Flegrei (C1 = 1st

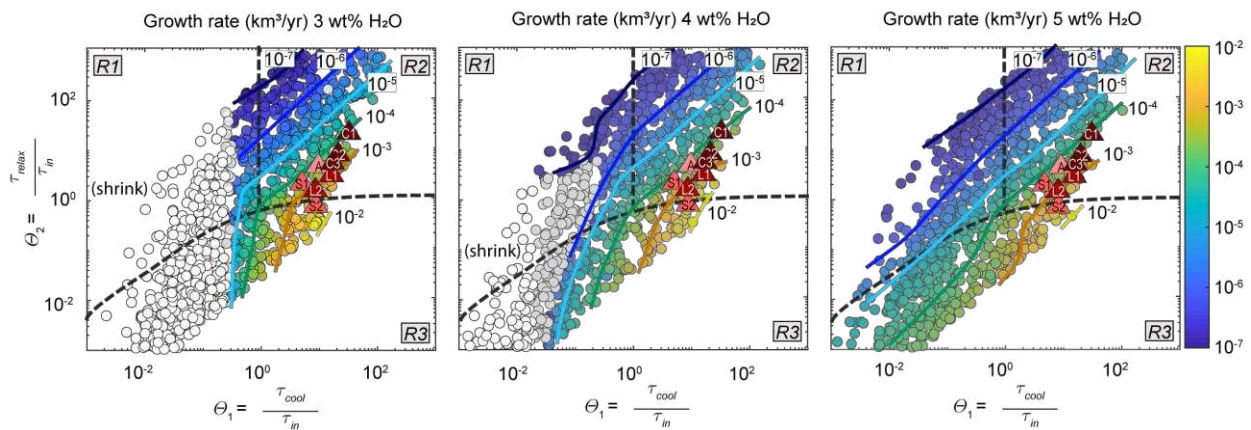
542 epoch, C2 = 2nd epoch, C3 = 3rd epoch), Santorini (S1 = post-Minoan period, S2 = pre-Minoan), and Aso (A1 =
 543 Phase 1, and A2 = Phase 2).

544

545 Model results show that chamber growth by volume follows a different trend than growth
 546 by mass. Although in the wet case we see mass loss where eruptions are triggered by second
 547 boiling, the volumes of the chambers remain constant because of the exsolution of the low-
 548 density MVP. In the dry case, in Regions 1 and 3 for which $\tau_{cool} < \tau_{in}$ and no eruptions occur,
 549 crystallization increases the bulk density and the volume of the chamber shrinks (Fig. 5d).

550 One of the outstanding questions in volcanology is how long it takes for chambers to build
 551 up to the caldera stage, and what governs this timescale. From the model results, we calculated
 552 volumetric growth rates by averaging the changes in chamber volume over the duration of the
 553 model simulation, i.e. until $\epsilon_x = 50\%$ (Figure 6). We find that the growth rate varies by over 5
 554 orders of magnitude across the regime diagrams, increasing to the bottom right from $\sim 10^{-7}$ km³/yr
 555 where θ_2 is large and θ_1 is small, up to $\sim 10^{-2}$ km³/yr where θ_2 is small while θ_1 is large. There are
 556 no significant differences in growth rates as a function of water content, except where $\theta_1 < 1$ and
 557 no growth is possible for the dry cases. The volcanic systems of interest all tend to plot along a
 558 contour of similar growth rate equal to about 10^{-3} km³/yr (Figure 6).

559



560

561

562 **Figure 6.** Growth rates calculated from model results, in km³/yr. White points refer to cases where volume either
 563 shrinks or remains constant. Shaded triangles represent the volcanic systems of Laguna del Maule (L1 = Early post-
 564 glacial period; L2 = Holocene), Campi Flegrei (C1 = 1st epoch, C2 = 2nd epoch, C3 = 3rd epoch), Santorini (S1 =
 565 post-Minoan period, S2 = pre-Minoan), and Aso (A1 = Phase 1, and A2 = Phase 2).

566 4. Discussion

567 4.1 Interplay of extrusive:intrusive ratio, eruption frequency, and chamber

568 *growth*

569 At the most basic level, magma chambers will grow when $M_{er}:M_{add} < 1$ and shrink when
570 $M_{er}:M_{add} > 1$, but why shouldn't the mass of magma erupted simply equal the mass of magma
571 added? Divergence from $M_{er}:M_{add} = 1$ occurs when irreversible processes – viscous relaxation
572 and phase changes during cooling – change how fast pressure can build or drop between and
573 during eruptions. This can be understood better by considering the change in chamber pressure
574 resulting from mass inflow and eruption:

575

$$576 \quad \beta \frac{dP}{dt} = \frac{\dot{M}_{in} - \dot{M}_{out}}{\rho V} - \frac{\Delta P}{\eta_r} \quad (11)$$

577

578 where the last term accounts for viscous relaxation of the crust and $\Delta P = P(t) - P_{lit}$. If we
579 integrate over a single eruption cycle and decompose the pressure evolution into the period
580 between and during the eruption, we find the total change in mass of the chamber during one
581 eruption cycle:

582

$$583 \quad \Delta M = \int_{repose} \rho V \beta \frac{dP}{dt} dt + \int_{eruption} \rho V \beta \frac{dP}{dt} dt + \int_{repose} \frac{\rho V \Delta P}{\eta_r} dt + \int_{eruption} \frac{\rho V \Delta P}{\eta_r} dt \quad (12)$$

584

585 The viscous response during the eruption can be neglected because the eruption duration
586 is small compared to the repose time ($1/f$):

587

$$588 \quad \Delta M \approx \langle \rho V \beta \rangle_{repose} \Delta P_c - \langle \rho V \beta \rangle_{eruption} \Delta P_c + \langle \rho V \eta_r^{-1} \rangle_{repose} \Delta P f^{-1} \quad (13)$$

589

590 where $\langle \rho V \beta \rangle$ indicates the average values of magma density, chamber volume, and
591 magma compressibility during the repose or eruption phase. From eq. (13), we can see one way
592 in which eruption frequency affects chamber growth; a longer repose time (lower eruption
593 frequency) allows greater mass accumulation by viscous deformation of the crust. If viscous

594 relaxation dominates, for example in Region 3 where no eruptions occur and the second term is
595 zero (Fig. 1), magma recharge always leads to chamber growth.

596 It is possible for a magma chamber being constantly recharged to shrink. If eruption
597 frequency is high or if η_r is very large (e.g. Regions 1 and 2 where $\theta_2 > 10$, Fig. 1), the viscous
598 term in eq. (13) may be neglected and a chamber will shrink by mass if $\langle \rho V \beta \rangle_{eruption} >$
599 $\langle \rho V \beta \rangle_{repose}$. Between eruptions, cooling and crystallization leads to second boiling, which
600 increases the value of β (eq. 4) such that it takes on a greater value at the initiation of an eruption
601 and $\langle \rho V \beta \rangle_{eruption} > \langle \rho V \beta \rangle_{repose}$. As a result, the mass lost during the eruption is greater than
602 the mass added during repose and the chamber shrinks, a result that is consistent with previous
603 work on the effect of volatiles on eruption size and frequency ([Bower & Woods, 1997](#); [Huppert](#)
604 [& Woods, 2002](#); [Woods & Huppert, 2003](#)). As eruption frequency increases and there is less
605 time between eruptions for second boiling (θ_1 increasing), the discrepancy between $\langle \rho V \beta \rangle_{repose}$
606 and $\langle \rho V \beta \rangle_{eruption}$ decreases and the mass balance approaches a neutral budget, i.e. less
607 shrinking occurs (Fig. 5c).

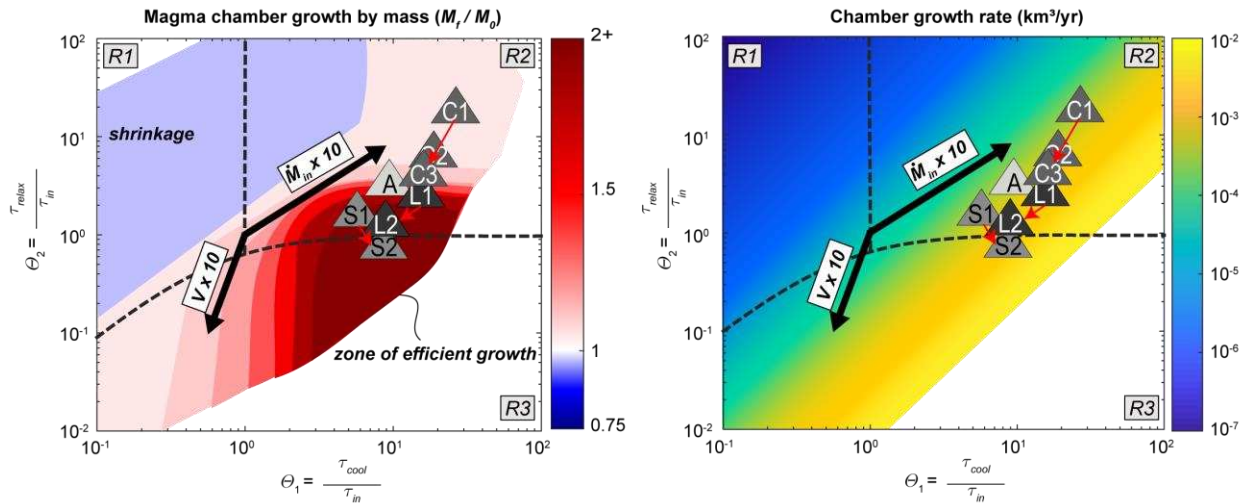
608 A key distinction we draw from the numerical results is the difference between growth by
609 mass and volume. While a non-eruptive chamber will always grow by mass when supplied with
610 magma, if the cooling rate outpaces injection ($\tau_{cool} < \tau_{in}$), crystallization and volatile exsolution
611 can change the bulk density of the magma. In dry cases (e.g. Fig. 5a and d), crystallization
612 dominates and the density increases, leading to volumetric shrinkage. In sufficiently wet systems
613 (e.g. Fig. 5c and f), exsolution balances this and the volume can remain constant or even
614 increase.

615 Overall, growth by both mass and volume is favored when injection and crustal
616 relaxation are both fast compared to cooling, highlighted by a zone in the bottom-right of the
617 regime space spanning $\sim \theta_1 = 1 - 50$ and $\sim \theta_2 = 0.05 - 5$ (Figure 7a). Within this “zone of
618 efficient growth”, growth is rapid and appears to be decoupled from eruption frequency, as it
619 intersects both Region 2, where hundreds or more eruptions can occur before the chamber
620 freezes, and Region 3 where no eruptions are expected to occur (Fig. 1). In other words, there is
621 a narrow zone where magma recharge is just faster than relaxation but much faster than cooling,
622 where chambers can simultaneously erupt and grow. The values of θ_1 and θ_2 estimated for the
623 volcanic epochs of Laguna del Maule, Campi Flegrei, post-caldera Santorini, and Aso all plot
624 within this zone of simultaneous eruption and growth, suggesting that during flare-ups of

625 volcanic activity, the underlying chambers are actually growing (Fig. 7). The pre-Minoan magma
 626 chamber at Santorini falls in Region 3 (no eruptions expected) primarily due to its large size (~50
 627 km³), suggesting that the Minoan eruption may have been triggered by a shift towards greater
 628 magma recharge rates leading up to the eruption ([Druitt et al., 2012](#)).

629

630



631

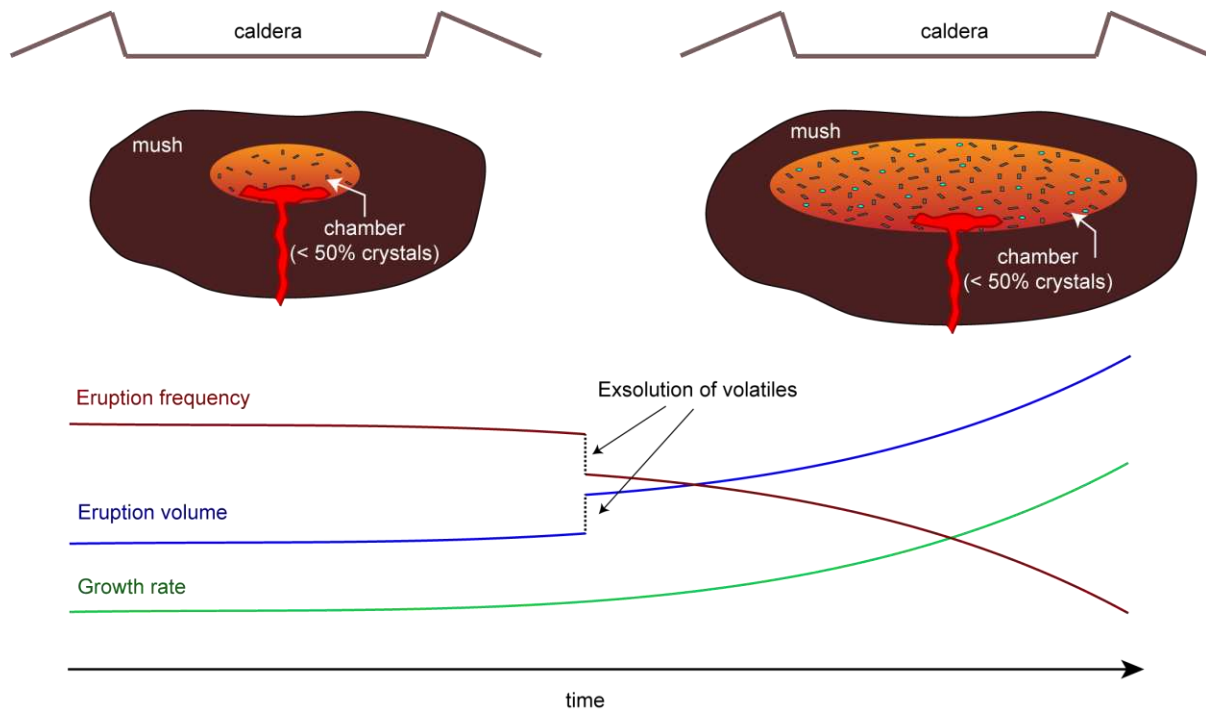
632 **Figure 7.** Trajectories of θ_1 and θ_2 in regime space taken as chambers progress along the caldera cycle. Bold black
 633 arrows provide an “uncertainty” related to model parameters: the length and direction of the arrows indicate how a
 634 system would shift in regime space if the chamber volume or mass inflow rate were different by one order of
 635 magnitude. Left panel: Magma chamber growth by mass, for 5 wt% water. Right panel: Chamber growth rates, for 5
 636 wt% water. Shaded triangles represent the volcanic systems of Laguna del Maule (L1 = Early post-glacial period; L2
 637 = Holocene), Campi Flegrei (C1 = 1st epoch, C2 = 2nd epoch, C3 = 3rd epoch), Santorini (S1 = post-Minoan period,
 638 S2 = pre-Minoan), and Aso (A1 = Phase 1, and A2 = Phase 2).

639

640 4.2 How do small chambers grow?

641 The model results suggest that growth is favored by larger chambers, and that smaller
 642 chambers will erupt frequently and grow more slowly. We explore how small chambers grow to
 643 the sizes required to produce massive caldera-forming eruptions by considering how the
 644 timescales for injection, cooling, and viscous relaxation evolve during growth. The non-
 645 dimensional quantities θ_1 and θ_2 are defined by the initial conditions of the magma chamber. In
 646 fact, these quantities evolve as the chamber grows, and in real systems they would further evolve
 647 as mass supply rate fluctuates and as the temperature of the host rock evolves ([Karakas,](#)
 648 [Degruyter, Bachmann, & Dufek, 2017](#)). In the regime space, growth of the chamber would cause
 649 θ_1 to decrease as $V^{-1/3}$ and θ_2 to decrease as V^{-1} , represented by one of the bold arrows in Figure

650 7. As the chamber grows and moves along this trajectory, it moves toward regions in which
 651 growth is encouraged and growth rates increase (Fig.7b). This suggests that the chamber volume
 652 should increase nonlinearly in time, growing faster as the chamber gets larger (Fig. 8). In
 653 addition, this implies that over time, even though eruptions should increase in size because of a
 654 larger chamber, the ratio of magma erupted to added will decrease overall.



655
 656 **Figure 8.** Conceptual model for the growth of subvolcanic magma chambers during inter-caldera periods, and
 657 associated changes in eruption frequency and volume. When magma chambers are small, eruptions are relatively
 658 frequent but small in volume, and the rate of growth of the chamber is slow but positive. Eventually as the chamber
 659 increases in size, growth rates increase, and eruptions become larger and less frequent. Exsolution of volatiles results
 660 in an increase of magma compressibility, suppressing eruption frequency and encouraging larger-volume eruptions.
 661

662 The volcanic systems of Laguna del Maule, Campi Flegrei, and to some extent Santorini
 663 all evolve along the trajectory of increasing volume during inter-caldera periods (Fig. 7). For
 664 example, the eruptible portion of the Campi Flegrei magma reservoir during Epoch 1 (“C1” in
 665 Fig. 7) is inferred to have been relatively small ($\sim 2.5 \text{ km}^3$) compared to the sizes of its largest
 666 eruptions (~ 40 and 300 km^3). According to the model results presented here, growth during this
 667 time may have been as slow as $\sim 3 \cdot 10^{-4} \text{ km}^3/\text{yr}$, which if kept constant (assuming an effective
 668 average mass recharge) would add $\sim 2 \text{ km}^3$ to the chamber by the time of Epoch 2 ~ 6000 years
 669 later. By Epoch 3, however, the chamber was larger and the growth rate may have been as fast as

670 $\sim 10^{-3}$ km³/yr. At that rate, it would take $\sim 30,000$ years to grow to the size of the Neapolitan
671 Yellow Tuff, which is roughly the amount of time between the eruptions of the two most recent
672 caldera-forming eruptions of the Campanian Ignimbrite and the Neapolitan Yellow Tuff.

673 We note, however, that the initial size and magma supply rates of the Campi Flegrei
674 system during Epoch 1 place it within the regime space where growth already is favored (Fig.
675 7a). For magma chambers initially much smaller than ~ 1 km³, growth is not expected to be
676 significant and the trajectory through the regime space due to changes in volume would be much
677 smaller than the trajectories illustrated by the volcanic systems presented here. In order for very
678 small systems (< 1 km³) to move toward conditions favorable for growth, another mechanism
679 may be required, such as a decrease in the host-rock viscosity, which would shift the trajectory
680 vertically down towards regions of increased growth. In reality, growth during the incipient
681 stages of chamber formation is probably encouraged by some combination of increasing magma
682 supply rates and decreasing host-rock viscosity as the crust warms up, and these processes are
683 important targets for future research. From the analysis presented here, we hypothesize that
684 while growth may be limited in the early stages of chamber formation, if a chamber reaches a
685 critical volume (in this model ~ 1 km³), growth becomes encouraged and the rate of growth can
686 speed up over time (Fig. 8).

687

688 **6. Conclusions**

689 Deposits from long-lived, caldera-forming volcanic systems such as Laguna del Maule,
690 Campi Flegrei, Santorini, and Aso suggest that silicic magma chambers can grow from a few
691 km³ to hundreds of km³ or more in the span of tens to hundreds of thousands of years. Here we
692 use a thermo-mechanical magma chamber model to examine conditions that would promote the
693 growth of these systems from the post- to pre-caldera stage. We find that growth is optimized
694 when the timescale for magma injection is short compared to the timescale for chamber cooling
695 ($\theta_1 > 1$), and when the timescale for viscous relaxation of the crust is comparable to the
696 timescale for injection ($\theta_2 \sim 1$). Within this “zone of efficient growth,” if the viscous relaxation
697 timescale is just shorter than the injection timescale ($\theta_2 < 1$), no eruptions occur and all magma
698 supplied to the system is stored within the chamber. If the viscous relaxation timescale is just
699 longer than the injection timescale ($\theta_2 > 1$), growth is accompanied by multiple volcanic

700 eruptions, which is expected to be the case for Laguna del Maule, Campi Flegrei, Santorini, and
701 Aso. We interpret this to mean that flare-ups in volcanic activity during inter-caldera periods at
702 these volcanoes may actually signal growth of the underlying chamber.

703 In summary, growth rates may initially be slow ($\sim 10^{-4}$ km³/yr), when magma chambers
704 are small (~ 1 km³), but as the chamber grows, this rate increases nonlinearly (Fig. 8). For
705 systems that both grow and erupt, chamber growth corresponds to changes in the frequency and
706 size of volcanic eruptions, such that frequency decreases and eruption volume increases in
707 proportion with chamber volume (Fig. 8). In addition, exsolution of magmatic volatiles can
708 increase the bulk compressibility of the magma, leading to proportional decreases in eruption
709 frequency and increases in eruption volume (Fig. 8). Altogether, the scaling for eruption
710 frequency and eruption volume as a function of chamber volume, magma supply rate, and
711 magma compressibility (state of volatile saturation) compare well with observations from
712 Laguna del Maule, Campi Flegrei, Santorini, and Aso, which supports the use of the volcanic
713 record to probe conditions and growth rates of underlying magma chambers.

714

715 **Acknowledgements**

716 Funding for this research was provided in part by grants from the National Science Foundation,
717 NSF EAR (1760004) to Townsend and Huber, NSF Integrated Earth System EAR (1411724) to
718 Huber. Bachmann acknowledges support from Swiss SNF grant # 200021_178928. All data from
719 the volcanic systems come from published literature and are included in Table 2. Please refer to
720 the supporting information for the input and output files for all model simulations.
721

722 **References**

- 723 Andersen, N. L., Singer, B. S., Costa, F., Fournelle, J., Herrin, J. S., & Fabbro, G. N. (2018).
724 Petrochronologic perspective on rhyolite volcano unrest at Laguna del Maule, Chile.
725 *Earth and Planetary Science Letters*, 493, 57-70. doi:10.1016/j.epsl.2018.03.043
726 Andersen, N. L., Singer, B. S., Jicha, B. R., Beard, B. L., Johnson, C. M., & Licciardi, J. M.
727 (2017). Pleistocene to Holocene Growth of a Large Upper Crustal Rhyolitic Magma
728 Reservoir beneath the Active Laguna del Maule Volcanic Field, Central Chile. *Journal of*
729 *Petrology*, 58(1), 85-114. doi:10.1093/petrology/egx006
730 Annen, C. (2009). From plutons to magma chambers: Thermal constraints on the accumulation
731 of eruptible silicic magma in the upper crust. *Earth and Planetary Science Letters*, 284(3-
732 4), 409-416. doi:10.1016/j.epsl.2009.05.006

733 Barton, M., & Huijsmans, J. P. P. (1986). Post-caldera dacites from the Santorini volcanic
734 complex, Aegean Sea, Greece -- an examples of the eruption of lavas of near-constant
735 composition over a 2,200 year period. *Contributions to Mineralogy and Petrology*, 94(4),
736 472-495. doi:10.1007/bf00376340

737 Bevilacqua, A., Bursik, M., Patra, A., Pitman, E. B., Yang, Q. Y., Sangani, R., & Kobs-
738 Nawotniak, S. (2018). Late Quaternary Eruption Record and Probability of Future
739 Volcanic Eruptions in the Long Valley Volcanic Region (CA, USA). *Journal of*
740 *Geophysical Research-Solid Earth*, 123(7), 5466-5494. doi:10.1029/2018jb015644

741 Bevilacqua, A., Flandoli, F., Neri, A., Isaia, R., & Vitale, S. (2016). Temporal models for the
742 episodic volcanism of Campi Flegrei caldera (Italy) with uncertainty quantification.
743 *Journal of Geophysical Research-Solid Earth*, 121(11), 7821-7845.
744 doi:10.1002/2016jb013171

745 Black, B. A., & Manga, M. (2016). The eruptibility of magmas at Tharsis and Syrtis Major on
746 Mars. *Journal of Geophysical Research-Planets*, 121(6), 944-964.
747 doi:10.1002/2016je004998

748 Black, B. A., & Manga, M. (2017). Volatiles and the tempo of flood basalt magmatism. *Earth*
749 *and Planetary Science Letters*, 458, 130-140. doi:10.1016/j.epsl.2016.09.035

750 Blake, S. (1984). Volatile oversaturation during the evolution of silicic magma chambers as an
751 eruption trigger. *Journal of Geophysical Research*, 89(NB10), 8237-8244.
752 doi:10.1029/JB089iB10p08237

753 Bower, S. M., & Woods, A. W. (1997). Control of magma volatile content and chamber depth on
754 the mass erupted during explosive volcanic eruptions. *Journal of Geophysical Research-*
755 *Solid Earth*, 102(B5), 10273-10290. doi:10.1029/96jb03176

756 Cadoux, A., Scaillet, B., Druitt, T. H., & Deloule, E. (2014). Magma Storage Conditions of
757 Large Plinian Eruptions of Santorini Volcano (Greece). *Journal of Petrology*, 55(6),
758 1129-1171. doi:10.1093/petrology/egu021

759 Calo, M., & Tramelli, A. (2018). Anatomy of the Campi Flegrei caldera using Enhanced Seismic
760 Tomography Models. *Scientific Reports*, 8. doi:10.1038/s41598-018-34456-x

761 Caricchi, L., Annen, C., Blundy, J., Simpson, G., & Pinel, V. (2014). Frequency and magnitude
762 of volcanic eruptions controlled by magma injection and buoyancy. *Nature Geoscience*,
763 7(2), 126-130. doi:10.1038/ngeo2041

764 Chamberlain, K. J., Wilson, C. J. N., Wooden, J. L., Charlier, B. L. A., & Ireland, T. R. (2014).
765 New Perspectives on the Bishop Tuff from Zircon Textures, Ages and Trace Elements.
766 *Journal of Petrology*, 55(2), 395-426. doi:10.1093/petrology/egt072

767 Charlier, B. L. A., Wilson, C. J. N., & Davidson, J. P. (2008). Rapid open-system assembly of a
768 large silicic magma body: time-resolved evidence from cored plagioclase crystals in the
769 Oruanui eruption deposits, New Zealand. *Contributions to Mineralogy and Petrology*,
770 156(6), 799-813. doi:10.1007/s00410-008-0316-y

771 Christiansen, R. L. (2001). *The Quaternary and Pliocene Yellowstone Plateau Volcanic Field of*
772 *Wyoming, Idaho, and Montana*. U.S. Geological Survey Professional Paper.

773 Cottrell, E., Gardner, J. E., & Rutherford, M. J. (1999). Petrologic and experimental evidence for
774 the movement and heating of the pre-eruptive Minoan rhyodacite (Santorini, Greece).
775 *Contributions to Mineralogy and Petrology*, 135(4), 315-331.
776 doi:10.1007/s004100050514

777 de Silva, S. L., & Gregg, P. M. (2014). Thermomechanical feedbacks in magmatic systems:
778 Implications for growth, longevity, and evolution of large caldera-forming magma

779 reservoirs and their supereruptions. *Journal of Volcanology and Geothermal Research*,
780 282, 77-91. doi:10.1016/j.jvolgeores.2014.06.001

781 Degruyter, W., & Huber, C. (2014). A model for eruption frequency of upper crustal silicic
782 magma chambers. *Earth and Planetary Science Letters*, 403, 117-130.
783 doi:10.1016/j.epsl.2014.06.047

784 Degruyter, W., Huber, C., Bachmann, O., Cooper, K. M., & Kent, A. J. R. (2016). Magma
785 reservoir response to transient recharge events: The case of Santorini volcano (Greece).
786 *Geology*, 44(1), 23-26. doi:10.1130/g37333.1

787 Degruyter, W., Huber, C., Bachmann, O., Cooper, K. M., & Kent, A. J. R. (2017). Influence of
788 Exsolved Volatiles on Reheating Silicic Magmas by Recharge and Consequences for
789 Eruptive Style at Volcan Quizapu (Chile). *Geochemistry Geophysics Geosystems*, 18(11),
790 4123-4135. doi:10.1002/2017gc007219

791 Deino, A. L., Orsi, G., de Vita, S., & Piochi, M. (2004). The age of the Neapolitan Yellow Tuff
792 caldera-forming eruption (Campi Flegrei caldera Italy) assessed by Ar-40/Ar-39 dating
793 method. *Journal of Volcanology and Geothermal Research*, 133(1-4), 157-170.
794 doi:10.1016/s0377-0273(03)00396-2

795 Del Negro, C., Currenti, G., & Scandura, D. (2009). Temperature-dependent viscoelastic
796 modeling of ground deformation: Application to Etna volcano during the 1993-1997
797 inflation period. *Physics of the Earth and Planetary Interiors*, 172(3-4), 299-309.
798 doi:10.1016/j.pepi.2008.10.019

799 Di Vito, M. A., Acocella, V., Aiello, G., Barra, D., Battaglia, M., Carandente, A., . . . Terrasi, F.
800 (2016). Magma transfer at Campi Flegrei caldera (Italy) before the 1538 AD eruption.
801 *Scientific Reports*, 6. doi:10.1038/srep32245

802 Di Vito, M. A., Isaia, R., Orsi, G., Southon, J., de Vita, S., D'Antonio, M., . . . Piochi, M. (1999).
803 Volcanism and deformation since 12,000 years at the Campi Flegrei caldera (Italy).
804 *Journal of Volcanology and Geothermal Research*, 91(2-4), 221-246. doi:10.1016/s0377-
805 0273(99)00037-2

806 Dragoni, M., & Magnanensi, C. (1989). Displacement and stress produced by a pressurized,
807 spherical magma chamber, surrounded by a viscoelastic shell. *Physics of the Earth and
808 Planetary Interiors*, 56(3-4), 316-328. doi:10.1016/0031-9201(89)90166-0

809 Druitt, T. H., Costa, F., Deloule, E., Dungan, M., & Scaillet, B. (2012). Decadal to monthly
810 timescales of magma transfer and reservoir growth at a caldera volcano. *Nature*,
811 482(7383), 77-U97. doi:10.1038/nature10706

812 Druitt, T. H., & Francaviglia, V. (1992). Caldera formation on Santorini and the physiography of
813 the islands in the Late Bronze Age. *Bulletin of Volcanology*, 54(6), 484-493.
814 doi:10.1007/bf00301394

815 Druitt, T. H., Mellors, R. A., Pyle, D. M., & Sparks, R. S. J. (1989). Explosive volcanism on
816 Santorini, Greece. *Geological Magazine*, 126(2), 95-126.
817 doi:10.1017/s0016756800006270

818 Druitt, T. H., Mercier, M., Florentin, L., Deloule, E., Cluzel, N., Flaherty, T., . . . Cadoux, A.
819 (2016). Magma Storage and Extraction Associated with Plinian and Interplinian Activity
820 at Santorini Caldera (Greece). *Journal of Petrology*, 57(3), 461-494.
821 doi:10.1093/petrology/egw015

822 Dufek, J., & Bergantz, G. W. (2005). Transient two-dimensional dynamics in the upper conduit
823 of a rhyolitic eruption: A comparison of closure models for the granular stress. *Journal of*

824 *Volcanology and Geothermal Research*, 143(1-3), 113-132.
825 doi:10.1016/j.jvolgeores.2004.09.013

826 Fedi, M., Cella, F., D'Antonio, M., Florio, G., Paoletti, V., & Morra, V. (2018). Gravity
827 modeling finds a large magma body in the deep crust below the Gulf of Naples, Italy.
828 *Scientific Reports*, 8. doi:10.1038/s41598-018-26346-z

829 Feigl, K. L., Le Mevel, H., Ali, S. T., Cordova, L., Andersen, N. L., DeMets, C., & Singer, B. S.
830 (2014). Rapid uplift in Laguna del Maule volcanic field of the Andean Southern Volcanic
831 zone (Chile) 2007-2012. *Geophysical Journal International*, 196(2), 885-901.
832 doi:10.1093/gji/ggt438

833 Flaherty, T., Druitt, T. H., Tuffen, H., Higgins, M. D., Costa, F., & Cadoux, A. (2018). Multiple
834 timescale constraints for high-flux magma chamber assembly prior to the Late Bronze
835 Age eruption of Santorini (Greece). *Contributions to Mineralogy and Petrology*, 173(9).
836 doi:10.1007/s00410-018-1490-1

837 Forni, F., Degruyter, W., Bachmann, O., De Astis, G., & Mollo, S. (2018). Long-term magmatic
838 evolution reveals the beginning of a new caldera cycle at Campi Flegrei. *Science*
839 *Advances*, 4(11). doi:10.1126/sciadv.aat9401

840 Gelman, S. E., Gutierrez, F. J., & Bachmann, O. (2013). On the longevity of large upper crustal
841 silicic magma reservoirs. *Geology*, 41(7), 759-762. doi:10.1130/g34241.1

842 Hata, M., Matsushima, N., Takakura, S., Utsugi, M., Hashimoto, T., & Uyeshima, M. (2018).
843 Three-dimensional electrical resistivity modeling to elucidate the crustal magma supply
844 system beneath Aso caldera, Japan. *Journal of Geophysical Research: Solid Earth*, 123.
845 doi:10.1029/2018JB015951

846 Hata, M., Takakura, S., Matsushima, N., Hashimoto, T., & Utsugi, M. (2016). Crustal magma
847 pathway beneath Aso caldera inferred from three-dimensional electrical resistivity
848 structure. *Geophysical Research Letters*, 43(20), 10720-10727.
849 doi:10.1002/2016gl070315

850 Hildreth, W. (1981). Gradients in silicic magma chambers -- implications for lithospheric
851 magmatism. *Journal of Geophysical Research*, 86(NB11), 153-192.
852 doi:10.1029/JB086iB11p10153

853 Hildreth, W., Godoy, E., Fierstein, J., & Singer, B. (2010). Laguna del Maule Volcanic Field:
854 Eruptive history of a Quaternary basalt-to-rhyolite distributed volcanic field on the
855 Andean range crest in central Chile. *Servicio Nacional de Geología y Minería -- Chile*, 63.

856 Huber, C., Bachmann, O., & Manga, M. (2009). Homogenization processes in silicic magma
857 chambers by stirring and mushification (latent heat buffering). *Earth and Planetary*
858 *Science Letters*, 283(1-4), 38-47. doi:10.1016/j.epsl.2009.03.029

859 Huppert, H. E., & Woods, A. W. (2002). The role of volatiles in magma chamber dynamics.
860 *Nature*, 420(6915), 493-495. doi:10.1038/nature01211

861 Jellinek, A. M., & DePaolo, D. J. (2003). A model for the origin of large silicic magma
862 chambers: precursors of caldera-forming eruptions. *Bulletin of Volcanology*, 65(5), 363-
863 381. doi:10.1007/s00445-003-0277-y

864 Johnston, E. N., Sparks, R. S. J., Phillips, J. C., & Carey, S. (2014). Revised estimates for the
865 volume of the Late Bronze Age Minoan eruption, Santorini, Greece. *Journal of the*
866 *Geological Society*, 171(4), 583-590. doi:10.1144/jgs2013-113

867 Kaneko, K., Kamata, H., Koyaguchi, T., Yoshikawa, M., & Furukawa, K. (2007). Repeated
868 large-scale eruptions from a single compositionally stratified magma chamber: An

869 example from Aso volcano, Southwest Japan. *Journal of Volcanology and Geothermal*
870 *Research*, 167(1-4), 160-180. doi:10.1016/j.jvolgeores.2007.05.002

871 Karakas, O., Degruyter, W., Bachmann, O., & Dufek, J. (2017). Lifetime and size of shallow
872 magma bodies controlled by crustal-scale magmatism. *Nature Geoscience*, 10(6), 446-+.
873 doi:10.1038/ngeo2959

874 Karlstrom, L., Dufek, J., & Manga, M. (2009). Organization of volcanic plumbing through
875 magmatic lensing by magma chambers and volcanic loads. *Journal of Geophysical*
876 *Research-Solid Earth*, 114. doi:10.1029/2009jb006339

877 Karlstrom, L., Dufek, J., & Manga, M. (2010). Magma chamber stability in arc and continental
878 crust. *Journal of Volcanology and Geothermal Research*, 190(3-4), 249-270.
879 doi:10.1016/j.jvolgeores.2009.10.003

880 Le Mevel, H., Gregg, P. M., & Feigl, K. L. (2016). Magma injection into a long-lived reservoir
881 to explain geodetically measured uplift: Application to the 2007-2014 unrest episode at
882 Laguna del Maule volcanic field, Chile. *Journal of Geophysical Research-Solid Earth*,
883 121(8), 6092-6108. doi:10.1002/2016jb013066

884 Lipman, P. W., Steven, T. A., & Mehnert, H. H. (1970). Volcanic history of San-Juan-
885 Mountains, Colorado, as indicated by potassium-argon dating. *Geological Society of*
886 *America Bulletin*, 81(8), 2329-&. doi:10.1130/0016-7606(1970)81[2329:vhotsj]2.0.co;2

887 Magee, C., Stevenson, C. T. E., Ebmeier, S. K., Keir, D., Hammond, J. O. S., Gottsmann, J. H., .
888 . . Jackson, M. D. (2018). Magma Plumbing Systems: A Geophysical Perspective.
889 *Journal of Petrology*, 59(6), 1217-1251. doi:10.1093/petrology/egy064

890 Matthews, N. E., Vazquez, J. A., & Calvert, A. T. (2015). Age of the Lava Creek supereruption
891 and magma chamber assembly at Yellowstone based on Ar-40/Ar-39 and U-Pb dating of
892 sanidine and zircon crystals. *Geochemistry Geophysics Geosystems*, 16(8), 2508-2528.
893 doi:10.1002/2015gc005881

894 McKee, C. O., Lowenstein, P. L., De Saint Ours, P., Talai, B., Itikarai, I., & Mori, J. J. (1984).
895 Seismic and ground deformation crises at Rabaul Caldera: Prelude to an eruption?
896 *Bulletin of Volcanology*, 47(2), 397-411.

897 Miller, C. A., Williams-Jones, G., Fournier, D., & Witter, J. (2017). 3D gravity inversion and
898 thermodynamic modelling reveal properties of shallow silicic magma reservoir beneath
899 Laguna del Maule, Chile. *Earth and Planetary Science Letters*, 459, 14-27.
900 doi:10.1016/j.epsl.2016.11.007

901 Miller, C. F., Furbish, D. J., Walker, B. A., Claiborne, L. L., Koteas, G. C., Bleick, H. A., &
902 Miller, J. S. (2011). Growth of plutons by incremental emplacement of sheets in crystal-
903 rich host: Evidence from Miocene intrusions of the Colorado River region, Nevada, USA.
904 *Tectonophysics*, 500(1-4), 65-77. doi:10.1016/j.tecto.2009.07.011

905 Miller, R. B., & Paterson, S. R. (2001). Construction of mid-crustal sheeted plutons: Examples
906 from the north Cascades, Washington. *Geological Society of America Bulletin*, 113(11),
907 1423-1442. doi:10.1130/0016-7606(2001)113<1423:comcsp>2.0.co;2

908 Miyabuchi, Y. (2009). A 90,000-year tephrostratigraphic framework of Aso Volcano, Japan.
909 *Sedimentary Geology*, 220(3-4), 169-189. doi:10.1016/j.sedgeo.2009.04.018

910 Miyoshi, M., Sumino, H., Miyabuchi, Y., Shinmura, T., Mori, Y., Hasenaka, T., . . . Nagao, K.
911 (2012). K-Ar ages determined for post-caldera volcanic products from Aso volcano,
912 central Kyushu, Japan. *Journal of Volcanology and Geothermal Research*, 229, 64-73.
913 doi:10.1016/j.jvolgeores.2012.04.003

- 914 Newman, A. V., Dixon, T. H., & Gourmelen, N. (2006). A four-dimensional viscoelastic
915 deformation model for Long Valley Caldera, California, between 1995 and 2000. *Journal*
916 *of Volcanology and Geothermal Research*, 150(1-3), 244-269.
917 doi:10.1016/j.jvolgeores.2005.07.017
- 918 Orsi, G., DeVita, S., & di Vito, M. (1996). The restless, resurgent Campi Flegrei nested caldera
919 (Italy): Constraints on its evolution and configuration. *Journal of Volcanology and*
920 *Geothermal Research*, 74(3-4), 179-214. doi:10.1016/s0377-0273(96)00063-7
- 921 Orsi, G., Di Vito, M. A., & Isaia, R. (2004). Volcanic hazard assessment at the restless Campi
922 Flegrei caldera. *Bulletin of Volcanology*, 66(6), 514-530. doi:10.1007/s00445-003-0336-4
- 923 Papadopoulos, G. A., Sachpazi, M., Panopoulou, G., & Stavrakakis, G. (1998). The
924 volcanoseismic crisis of 1996-97 in Nisyros, SE Aegean Sea, Greece. *Terra Nova*, 10(3),
925 151-154.
- 926 Parks, M. M., Biggs, J., England, P., Mather, T. A., Nomikou, P., Palamartchouk, K., . . .
927 Zacharis, V. (2012). Evolution of Santorini Volcano dominated by episodic and rapid
928 fluxes of melt from depth. *Nature Geoscience*, 5(10), 749-754. doi:10.1038/ngeo1562
- 929 Paterson, S. R., & Miller, R. B. (1998). Mid-crustal magmatic sheets in the Cascades Mountains,
930 Washington: implications for magma ascent. *Journal of Structural Geology*, 20(9-10),
931 1345-1363. doi:10.1016/s0191-8141(98)00072-8
- 932 Pyle, D. M., & Elliott, J. R. (2006). Quantitative morphology, recent evolution, and future
933 activity of the Kameni Islands volcano, Santorini, Greece. *Geosphere*, 2(5), 253-268.
934 doi:10.1130/ges00028.1
- 935 Rubin, A. M. (1995). Getting granite dikes out of the source region. *Journal of Geophysical*
936 *Research-Solid Earth*, 100(B4), 5911-5929. doi:10.1029/94jb02942
- 937 Segall, P. (2016). Re-pressurization following eruption from an magma chamber with a viscoelastic
938 aureole. *Journal of Geophysical Research-Solid Earth*, 121(12), 8501-8522.
939 doi:10.1002/2016jb013597
- 940 Sigurdsson, H., Carey, S., Alexandri, M., Vougioukalakis, G., Croff, K., Roman, C., . . .
941 Nomikou, P. (2011). Marine investigations of Greece's Santorini Volcanic Field. *Eos*
942 *(Transactions, American Geophysical Union)*, 87(34), 337-342.
- 943 Singer, B., Anderson, N., Le Mevel, H., Feigl, K., DeMets, C., Tikoff, B., . . . Vazquez, J.
944 (2014). Dynamics of a large, restless, rhyolitic magma system at Laguna del Maule,
945 southern Andes, Chile. *GSA today*, 24(12). doi:10.1130/GSATG216A.1
- 946 Singer, B., Le Mevel, H., Licciardi, J., Cordova, L., Tikoff, B., Garibaldi, N., . . . Feigl, K.
947 (2018). Geomorphic expression of rapid Holocene silicic magma reservoir growth
948 beneath Laguna del Maule, Chile. *Science Advances*, 4(6). doi:10.1126/sciadv.aat151
- 949 Smith, V. C., Isaia, R., & Pearce, N. J. G. (2011). Tephrostratigraphy and glass compositions of
950 post-15 kyr Campi Flegrei eruptions: implications for eruption history and
951 chronostratigraphic markers. *Quaternary Science Reviews*, 30(25-26), 3638-3660.
952 doi:10.1016/j.quascirev.2011.07.012
- 953 Snyder, D., & Tait, S. (1995). Replenishment of magma chambers: Comparison of fluid-
954 mechanic experiments with field relations. *Contributions to Mineralogy and Petrology*,
955 122(3), 230-240. doi:10.1007/s004100050123
- 956 Sparks, R. S. J., Francis, P. W., Hamer, R. D., Pankhurst, R. J., Ocallaghan, L. O., Thorpe, R. S.,
957 & Page, R. (1985). Ignimbrites of the Cerro Galan caldera, NW Argentina. *Journal of*
958 *Volcanology and Geothermal Research*, 24(3-4), 205-248. doi:10.1016/0377-
959 0273(85)90071-x

- 960 Stock, M., Humphreys, M., Smith, V., Isaia, R., Brooker, R., & Pyle, D. (2018). Tracking
961 Volatile Behaviour in Sub-volcanic Plumbing Systems Using Apatite and Glass:
962 Insights into Pre-eruptive Processes at Campi Flegrei, Italy. *Journal of Petrology*, 0, 1-29.
963 doi:10.1093/petrology/egy020
- 964 Stock, M. J., Humphreys, M. C. S., Smith, V. C., Isaia, R., & Pyle, D. M. (2016). Late-stage
965 volatile saturation as a potential trigger for explosive volcanic eruptions. *Nature*
966 *Geoscience*, 9(3), 249-U290. doi:10.1038/ngeo2639
- 967 Sudo, Y., & Kong, L. S. L. (2001). Three-dimensional seismic velocity structure beneath Aso
968 Volcano, Kyushu, Japan. *Bulletin of Volcanology*, 63(5), 326-344.
969 doi:10.1007/s004450100145
- 970 Tait, S., Jaupart, C., & Vergnolle, S. (1989). Pressure, gas content and eruption periodicity of a
971 shallow, crystallizing magma chamber. *Earth and Planetary Science Letters*, 92(1), 107-
972 123. doi:10.1016/0012-821x(89)90025-3
- 973 White, S. M., Crisp, J. A., & Spera, F. J. (2006). Long-term volumetric eruption rates and
974 magma budgets. *Geochemistry Geophysics Geosystems*, 7. doi:10.1029/2005gc001002
- 975 Wiebe, R. A. (1994). Silicic magma chambers as traps for basaltic magmas -- the Cadillac
976 Mountain intrusive complex, Mount Desert Island, Maine. *Journal of Geology*, 102(4),
977 423-437. doi:10.1086/629684
- 978 Wiebe, R. A., & Collins, W. J. (1998). Depositional features and stratigraphic sections in granitic
979 plutons: implications for the emplacement and crystallization of granitic magma. *Journal*
980 *of Structural Geology*, 20(9-10), 1273-1289. doi:10.1016/s0191-8141(98)00059-5
- 981 Wilson, C. J. N., Houghton, B. F., McWilliams, M. O., Lanphere, M. A., Weaver, S. D., &
982 Briggs, R. M. (1995). Volcanic and structural evolution of Taupo Volcanic Zone, New
983 Zealand -- a review. *Journal of Volcanology and Geothermal Research*, 68(1-3), 1-28.
984 doi:10.1016/0377-0273(95)00006-g
- 985 Woods, A. W., & Huppert, H. E. (2003). On magma chamber evolution during slow effusive
986 eruptions. *Journal of Geophysical Research-Solid Earth*, 108(B8).
987 doi:10.1029/2002jb002019
- 988 Zhang, Y. X. (1999). Exsolution enthalpy of water from silicate liquids. *Journal of Volcanology*
989 *and Geothermal Research*, 88(3), 201-207. doi:10.1016/s0377-0273(98)00115-2
- 990 Zollo, A., Maercklin, N., Vassallo, M., Dello Iacono, D., Virieux, J., & Gasparini, P. (2008).
991 Seismic reflections reveal a massive melt layer feeding Campi Flegrei caldera.
992 *Geophysical Research Letters*, 35(12). doi:10.1029/2008gl034242

993

994